Narodowe Centrum Badań Jądrowych
National Centre for Nuclear Research
ŚWIERK

REACTIVITY CONTROL BY THE PUMPING SYSTEM IN THE DUAL FLUID REACTOR

Mateusz Nowak

A thesis submitted in fulfillment of the requirements for the degree of Doctor of Physical Sciences in Department of Complex System

Supervisor:
Prof. dr hab. Konrad Czerski

Auxiliary supervisor:
dr Michał Spirzewski

15th June 2023

Acknowledgments

I would like to sincerely thank my supervisor, Prof. Konrad Czerski, for the scientific supervision, patience and support received in writing this thesis.

I would also like to sincerely thank my auxiliary supervisor Dr inż. Michal Spirzewski for his scientific supervision, infinite amount of patience, fruitful cooperation and support received in writing this thesis.

I would like to thank all my friends and colleagues who have always supported me in difficult times.

I would also like to thank my parents, my brother and my family for their constant support, their priceless suggestions and for helping me in difficult times when I needed it.

Contents

Nomenclature

Greek symbols

ρ	density, $\left(\frac{kg}{m^3}\right)$
ρ'	resistivity, $(\Omega \cdot m)$
ρ''	current density, $\left(\frac{A}{m^2}\right)$
μ	dynamic viscosity, $(mPa \cdot s)$
Φ	magnetic induction per duct area, $\left(\frac{T}{m^2}\right)$

Latin

B_m	magnetic induction, (T)
d	pump channel wall thickness, (m)
e	roughness, (-)
F	Lorentz force, (N)
f_d	friction factor, (-)
Ha	Hartmann number, (-)
H_d	pump height, (m)
I	supplied current, (A)
L	pump length, (m)
$\dot{m}$	mass flow (kg/s)
ΔP	pressure difference, (Pa)
Q	volumetric flow, $(\frac{m^3}{s})$
Re	Reynolds number, (-)
S	pump duct area, (m^2)
T	temperature, (K)

t	temperature, (^oC)
v	flow velocity, ($\frac{m}{s}$)
W_d	pump width, (m)

Subscripts

b	referring to bypass (frozen field)
d	referring to pump channel
ECM	referring to equivalent circuit method
EM	referring to electromagnetic
gain	referring to gain pressure
LM	referring to liquid metal
loop	referring to loop
loss	referring to pressure losses
MR	referring to multivariate regression
PA	referring to polynomial approximation
pump	referring to pump
SA	referring to simulated annealing
val	referring to validation
w	referring to pump channel wall

Acronyms

DFE	Dual Fluid Energy Inc.
DFR	Dual Fluid Reactor
ECM	Equivalent Circuit Method
FLIP	Flat Linear Induction Pump
HPR	Hot Pipe Microreactor
μDEMO	Microdemonstrator
mDEMO	Minidemonstrator
MHD	Magnetohydrodynamics
MR	Multivariate Regression

PA	Polynomial Approximation
SA	Simulated Annealing

Abstract

The DFR(m) reactor is a new nuclear reactor concept, and it is therefore necessary at the outset to create simplified models of this design so that appropriate tests and experiments can be carried out under safe, controlled conditions. Such test systems have been named demonstrators, and their purpose will be to conduct heat transfer and flow experiments.

One of the issues described in the thesis is the problem of scalability between demonstrators. The thesis examines whether, having the parameters of one device, it is possible to estimate the parameters of another. By developing such a method, it would be possible to predict the behavior of the DFR using the demonstrators. In the dissertation, it was proven that there is a possibility for demonstrators to be scalable using Nusselt number. The requirements are that the design of the microdemonstrator and the minidemonstrator are matched so that there is the same Nusselt number between the two devices.

The dissertation also focused on the effect of flow velocity on reactivity and heat transfer in demonstrators to prove that in liquid metal-based nuclear reactors, pumping systems also have a regulatory and control function. The Cathare-2 calculations presented here confirm that the flow velocity in the fuel and cooling loop affects heat transfer.

Since the working medium in the minidemonstrator, as well as in the final design of the DFR(m), will be liquid metals reaching high temperatures, it will not be possible to use pumps with internal components, as they may be eroded, corroded or otherwise damaged. Therefore, it was decided to use magnetohydrodynamic pumps, which are based on electromagnetic forcing of the conductive liquid, thus avoiding the aforementioned risks to the pumping system.

However, no one has designed and analyzed these devices for a Dual Fluid reactor with as many as two liquid metal loops. The work in this area is innovative and can be used in the design of other Generation IV reactors based on the use of liquid metals or molten salts. The dissertation presents the Equivalent Circuit Method analytical method and, based on it, optimizes the pump geometry for the DFR to minimize the pump supply current.

Streszczenie

Reaktor DFR(m) jest nową koncepcją reaktora jądrowego i dlatego na początku konieczne jest stworzenie uproszczonych modeli tego projektu, aby można było przeprowadzić odpowiednie testy i eksperymenty w bezpiecznych, kontrolowanych warunkach. Takie systemy testowe został nazwane demonstratorami, a ich celem będzie przeprowadzanie eksperymentów w zakresie wymiany ciepła i przepływu.

Jednym z zagadnień opisanych w pracy doktorskiej jest problem skalowalności pomiędzy demonstratorami. W pracy sprawdzono, czy posiadając parametry jednego z urządzeń istnieje możliwość oszacowania parametrów drugiego. Dzięki opracowaniu takiej metody, można byłoby za pomocą demonstratorów przewidzieć zachowanie DFR. W pracy doktorskiej udowodniono, że istnieje możliwość na skalowalność demonstratorów za pomocą liczby Nusselta. Warunkiem jest, aby konstrukcja mikrodemonstratora i minidemonstratora była tak dopasowana, aby pomiędzy dwoma urządzeniami była taka sama liczba Nusselta.

W pracy doktorskiej skupiono się także nad wpływem prędkości przepływu na reaktywność i wymianę ciepła w demonstratorach, aby udowodnić, że w reaktorach jądrowych opartych na ciekłych metalach, układy pompujące mają także funkcję regulacyjną i kontrolną. Przedstawione obliczenia Cathare-2 potwierdzają, że prędkość przepływu w pętli paliwowej i chłodzącej ma wpływ na wymianę ciepła.

Ze względu na fakt, że w minidemonstratorze, jak również w ostatecznej konstrukcji DFR(m), czynnikiem roboczym będą ciekłe metale osiągające wysokie temperatury, nie będzie możliwe zastosowanie pomp z wewnętrznymi komponentami, ponieważ mogą one ulec erozji, korozji lub innym uszkodzeniom. W związku z tym zdecydowano się na zastosowanie pomp magnetohydrodynamicznych, które opierają się na elektromagnetycznym wymuszaniu przepływu cieczy przewodzącej, unikając w ten sposób wspomnianych wcześniej zagrożeń dla układu pompowego.

Nikt jednak nie zaprojektował i nie przeanalizował tych urządzeń dla reaktora Dual Fluid z aż dwiema pętlami ciekłego metalu. Praca w tym obszarze jest innowacyjna i może być wykorzystana przy projektowaniu innych reaktorów IV generacji opartych na wykorzystaniu ciekłych metali lub stopionych soli. W pracy doktorskiej przedstawiono metodę analityczną Equivalent Circuit Method i na jej postawie zoptymalizowano geometrię pomp dla DFR pod kątem minimalizacji prądu zasilającego pompę.

Part I

Introduction and theoretical background

Chapter 1

Introduction

In Poland and the European Union, sustainable development of electricity and environmental protection are becoming increasingly important. For this reason, it was decided to reduce the use of fossil fuels and replace them with greener solutions. Renewable energy, namely solar, wind and hydroelectric power, is gaining a growing group of supporters. However, renewable energy alone cannot solve, the increasing demand of society and industry for electricity and heat. In addition, these energy sources are highly susceptible to weather and climate conditions. Energy storage methods are constantly being developed, however, they are too costly and not profitable to use in the energy economy. As a result, a strong chance has arisen for nuclear power.

The Dual Fluid Reactor (DFR) is a relatively new nuclear reactor concept. The patent application for DFR was approved in 2013 ([Huke et al., 2013]) and Its applicants are: A. Huke, R. Goetz, A. Hussein, K. Czerski and S. Gottlieb. The work on the concept is being carried out by the various institutes shown in the diagram 1.1. The main manager and investor in the DFR project is the Canadian company Dual Fluid Energy INC (DFE).

The story of the DFR reactor concept began in 2013, when a patent was created for a design with two loops - a fuel loop, where the working medium can be molten salt or liquid metal, and a liquid metal cooling loop [Huke et al., 2013]. The concept was then described in more detail in 2014 in an article [Huke et al., 2014]. Since then, two branches of the concept have been developed - on molten salts (sDFR) and a version based on liquid metals (mDFR) [Huke et al., 2015]. Subsequently, various studies related to neutronics ([Sierchuła et al., 2019], [Hanusek and Macian-Juan, 2022], [Sierchuła et al., 2022]), transient and steady-state reactor states ([Wang and Macian-Juan, 2018],[Wang et al., 2021b])

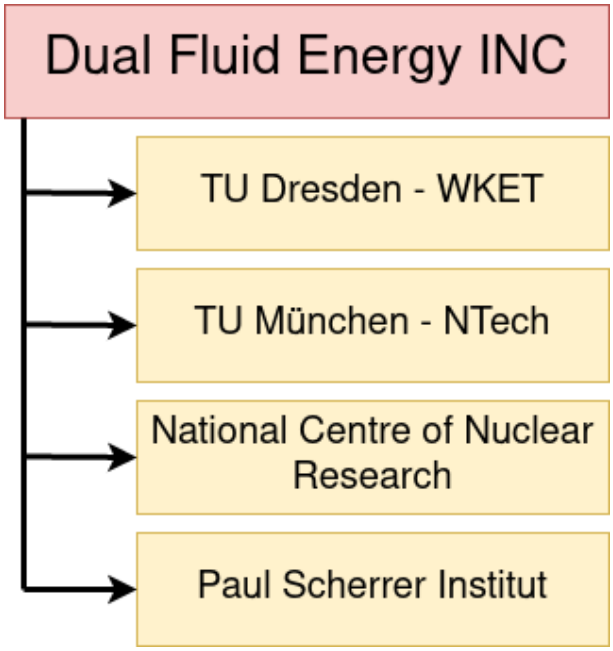

Figure 1.1: Diagram showing the institutes working with DFE in the design of the DFR.

were performed. The first thermohydraulic and CFD calculations related to DFR reactor flows also began to appear ([Wang et al., 2019],[Liu et al., 2022]). Works that differ significantly in subject matter, but are also of interest from a reactor perspective are [Weissbach et al., 2021], where the fission products that will occur in a DFR reactor are considered, as well as the first analyses of the pumping system for DFR [Nowak et al., 2022]. There was also an article about an alternative design based on the DFR concept - Heat Pipe Microreactor (HPR) [Miao et al., 2023]. The figure 1.2 shows a diagram summarizing the number and category of issued articles directly linked to the DFR.

This means that the topics of demonstrators and magnetohydrodynamic pumps have not yet been fully described. Therefore, these are two topics that are scientifically attractive and will be covered in this thesis.

Subsection 1.1 presents the path of nuclear power development, based on which the idea of a Dual Fluid Reactor was developed.

Subsection 1.2 presents the research motivation, as well as the research hypotheses, which are the main idea of all this work.

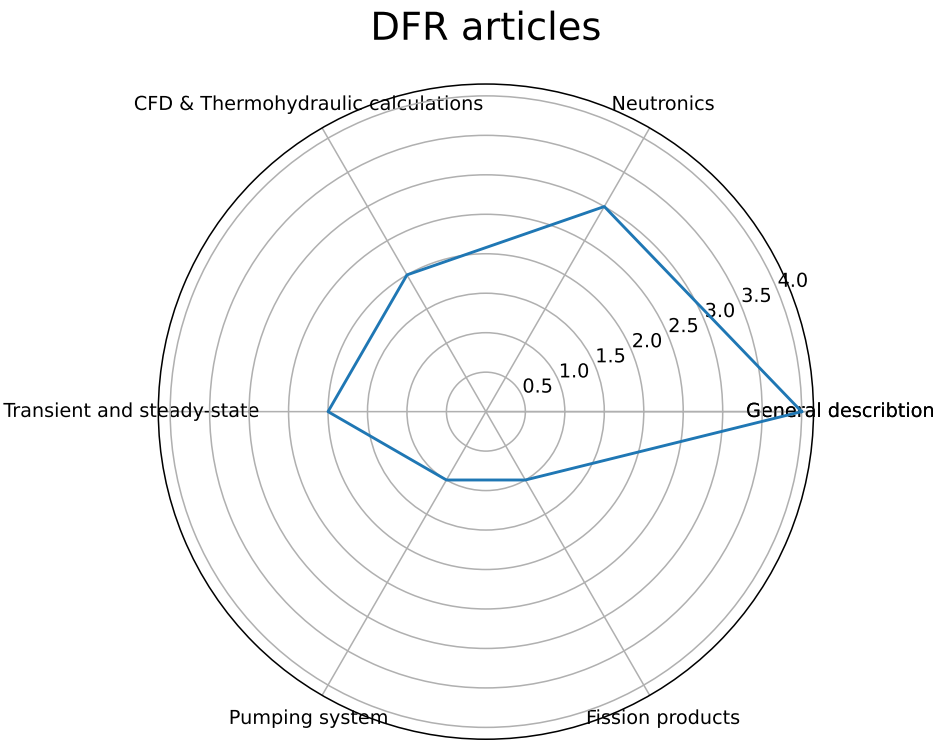

Figure 1.2: Radar diagram showing the number of publications written in a given category.

1.1 Research background

First generation nuclear reactors included the Pressurized Water Reactor (PWR) and Boiling Water Reactor (BWR). These devices were developed up to the third generation. However, increasing attention has been paid to the safety and efficiency of light-water reactor-based nuclear power. For this reason, a fourth generation of reactors based on less conventional coolants was started.

Sodium-cooled Fast Reactor (SFR) is a type of nuclear reactor that uses liquid sodium as coolant instead of conventional water. SFR also utilizes the fast neutron spectrum, which allows higher energy output than conventional water-cooled reactors [Singh, 2021].

In addition, SFR can operate at higher temperatures. This increases the efficiency of the power conversion system and reduces waste. Sodium has several advantages several advantages over water/steam/helium as a cooling medium. Due to its high boiling point

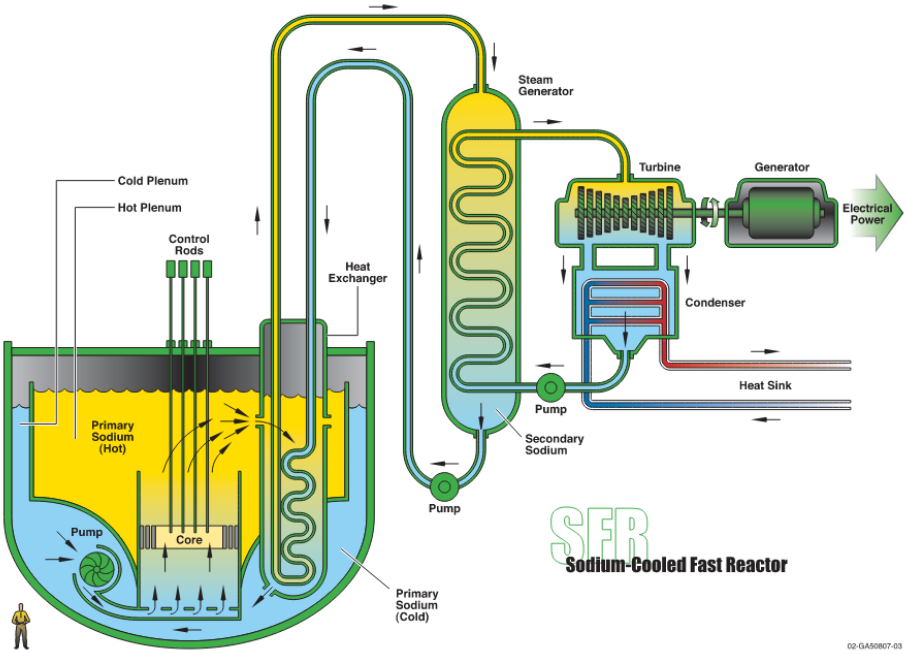

Figure 1.3: Scheme of SFR [Pioro, 2016].

and excellent heat transfer properties, it can transfer heat from the core to the power conversion system more efficiently than water. In addition, since sodium is less likely to be activated by neutron beams, the amount of radioactive waste generated will be reduced. SFRs also have some potential advantages over other types of reactors. For one, SFR's fast neutron spectrum allows the use of more abundant nuclear fuels like thorium, which may help reduce reliance on uranium [Pioro, 2016].

However, SFR also presents some challenges. Due to the high reactivity of sodium, advanced materials must be used that can withstand high temperatures and chemical attack. Additionally, sodium can ignite when exposed to air or water, creating a safety hazard if leaks occur.

Despite these challenges, SFRs are being researched and developed as a potential future energy source in the hope that they can provide a safer and more efficient alternative to conventional water-cooled nuclear reactors[Pioro, 2016].

Lead-cooled Fast Reactor (LFR) is a type of nuclear reactor that uses lead or lead-bismuth eutectic as coolant instead of conventional water [Singh, 2021]. LFR also uses the fast neutron spectrum, allowing higher energy output than conventional water-cooled reactors.

Lead has several advantages as a coolant. It has a high boiling point, does not react

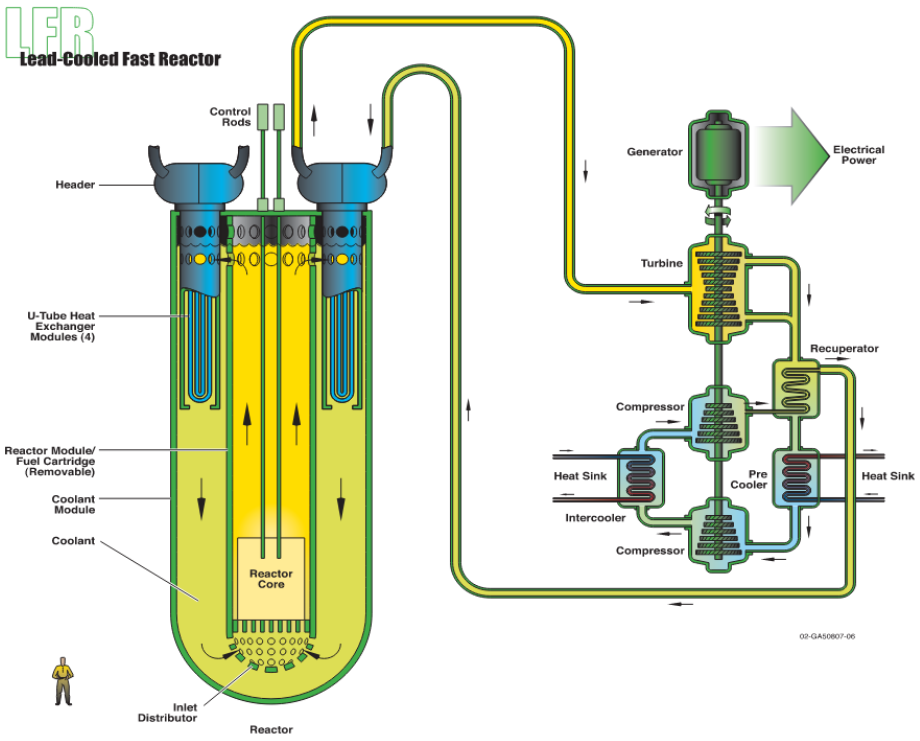

Figure 1.4: Scheme of LFR [Pioro, 2016].

with water or air, is not easy to leak, and is not easy to corrode. Additionally, lead has excellent heat transfer properties, allowing it to transfer heat from the core to the power conversion system more efficiently than water. LFRs also have some potential advantages over other types of reactors. For one, the LFR's fast neutron spectrum allows the use of more abundant nuclear fuels like thorium, which may help reduce reliance on uranium. In addition, the LFR can operate at higher temperatures. This increases the efficiency of the power conversion system and reduces waste[Pioro, 2016].

However, LFR also presents some challenges. Lead and lead-bismuth eutectic can be corrosive to some materials, so advanced materials must be used that can withstand high temperatures and radiation levels. Additionally, lead-based coolants can pose a safety hazard as lead can become radioactive when exposed to neutron radiation.

Despite these challenges, LFRs are being researched and developed as a potential future energy source in the hope that they can provide a safer and more efficient alternative to conventional water-cooled nuclear reactors. [Smith et al., 2008] [Alemberti et al., 2014]

Molten Salt Reactor (MSR) is a type of nuclear reactor that uses a liquid fuel mixture of nuclear fuel salts such as fluorides and chlorides that also act as coolant [Singh, 2021]. Unlike conventional nuclear reactors that use solid fuel rods and water

or gas coolants, MSR fuel dissolves in hot molten salts, allowing for efficient heat transfer and better control of reactions.

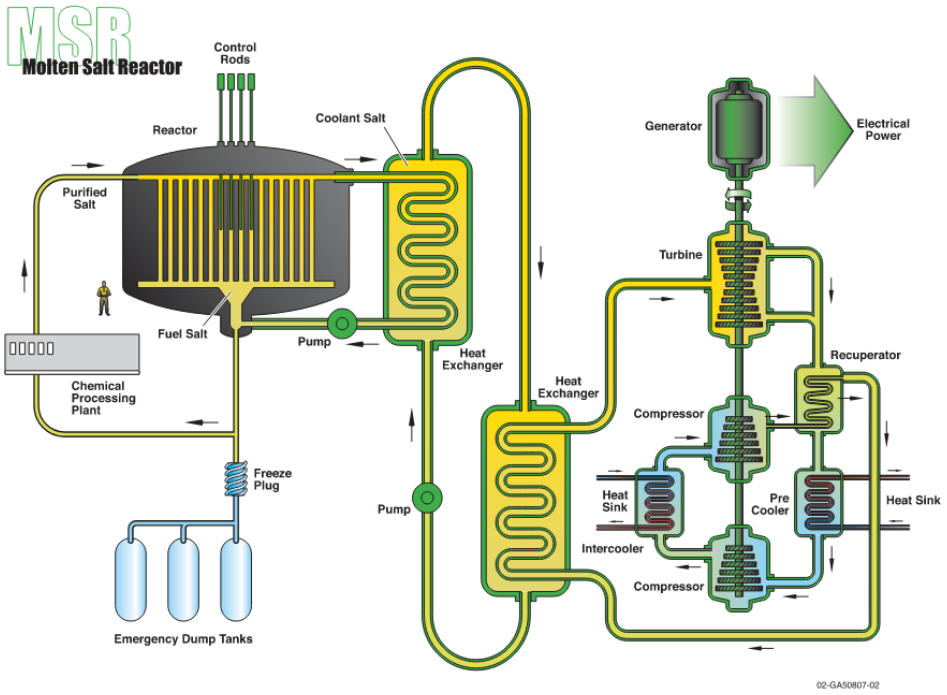

Figure 1.5: Scheme of MSR [Pioro, 2016].

MSRs have several potential advantages over other types of reactors. For one, the liquid fuel could be continuously circulated inside the reactor, allowing online refueling and potentially reducing the amount of radioactive waste produced. In addition, MSRs can operate at high temperatures, increasing the efficiency of power conversion systems and enabling the generation of high temperature industrial process heat. MSRs may also be able to use a wider range of nuclear fuels, including thorium and uranium-233, which are more abundant than the uranium-235 used in conventional nuclear reactors. This could help reduce reliance on uranium and make nuclear energy more sustainable [Serp et al., 2014].

However, MSR also presents some challenges. The corrosive nature of fuel mixtures requires the use of advanced materials that can withstand high temperatures and chemical attack. Liquid fuels also pose some safety risks as potential leaks and spills can lead to contamination and accidents. Despite these challenges, MSRs are being researched and developed as a potential future energy source in the hope that they can provide a safer and more efficient alternative to conventional nuclear reactors. [van Rooijen, 2009]

[Hejzlar et al., 2005]

Table 1.1: Summary of metallic nuclear reactor parameters based on [Becker et al., 2007]

	MSR	**SFR**	**LFR**
Coolant	15LiF + 58NaF + 27BeF	Na	LBE
Fuel type	Liquid TRU F_3	Metallic TRU in ZR matrix	Metallic TRU in ZR matrix
Power density	390 $\frac{W}{cm^3}$	332.54 $\frac{W}{cm}$	181.41 $\frac{W}{cm}$
Total reactor power [MWth]	750	840	840
Thermal fission $<$ 0.625 eV	0.2 %	0.0 %	0.0 %
Epithermal fission 0.625 eV - 100 keV	95.3 %	65.4 %	58.5 %
Fast fission $>$ 100 keV	4.5 %	34.6 %	41.5 %

In addition to the above-mentioned solutions, an additional nuclear reactor concept has been developed, called DFR (dual-fluid reactor). Among the advantages of DFR design is - higher energy density, very high neutron energies, so you can fission of not fertile trans isotopes of uranium: Pl^{240}, Am^{241}, on-line processing (distillation). The DFR will have a very high temperature, which is essential for hydrogen production, as well as for industry, self-regulation - the need for external power, rapid power reduction (minutes) to 7% (decay heat) at almost constant temperature (cooperation with renewable energy sources). In addition, the IROI factor for this type of reactor is much higher than for other light-water reactors, which is a significant advantage [Huke et al., 2015].

Because it uses liquid metals that are heated to high temperatures, conventional pumps cannot be used in the circuits, as the internal components could be damaged or corroded. It was therefore decided to use technology based on the use of electric and magnetic fields to move conductive liquid. The solution is magnetohydrodynamic (MHD) pumps, whose components do not need to be in contact with the high-temperature fluid.

1.2 Research motivation

The DFR(m) is a new nuclear reactor concept and therefore it is necessary to at the outset, simplified models of this design should be created so that appropriate tests and experiments can be carried out under safe, controlled conditions. One such test system has been named the minidemonstrator and its purpose will be to carry out heat transfer and flow experiments. Due to the fact that in the minidemonstrator, as well as in the final design of the DFR(m), the working medium will be liquid metals reaching high temperatures, it will

not be possible to use pumps with internal components, as they may be eroded, corroded or otherwise damaged. Therefore it was decided to use magnetohydrodynamic pumps, which are based on the electromagnetic forcing of a conductive fluid flow, thus avoiding the previously mentioned risks to the pumping system. A Dual Fluid Reactor consists of two loops in which liquid metals will flow. This means that due to the demanding operating media, a specialised pumping system such as magnetohydrodynamic pumps will have to be used. It is, therefore, necessary to analyse and design work on this equipment. Magnetohydrodynamic pumps are devices used in reactors where liquid metals have been used (such as a liquid sodium-cooled reactor or a liquid lead-cooled reactor). However, no one has designed and analyzed these devices for a Dual Fluid Reactor with as many as two liquid metal loops. The work in this area is innovative and could be used in the design of other Generation IV reactors based on the use of liquid metals or molten salts. The main idea of the thesis is that reactivity and heat transfer in a Dual Fluid Reactor can be controlled by the velocity of the liquid metal in the reactor core. Confirmation of this statement would prove that magnetohydrodynamic pumps have a control function in a DFR. To prove the hypothesis, it was decided to use Cathare-2 software, which is a system code. It is a tool in which other reactor types can be simulated, so it will be used for the calculations for the DFR's demonstrators. The magnetohydrodynamic pumps will also be simulated in the Cathare-2 software and, in addition, the analytical equivalent circuit method will be used for analysis and the simulation annealing meta-heuristic method will be used for optimisation.

The tasks that were performed in this dissertation can be divided into two separate cases. The first task is the problem of scalability between demonstrators, while the second is the design and optimization of a magnetohydrodynamic pump. However, despite the use of different tools, the main idea is to control the flow of liquid metal in the DFR core (figure 1.6). Therefore, the focus was on creating tools that can assist in the design of the pumping system in the DFR. Because DFR is a new concept, operating at very high temperatures, so the work consists mainly of mathematical calculations.

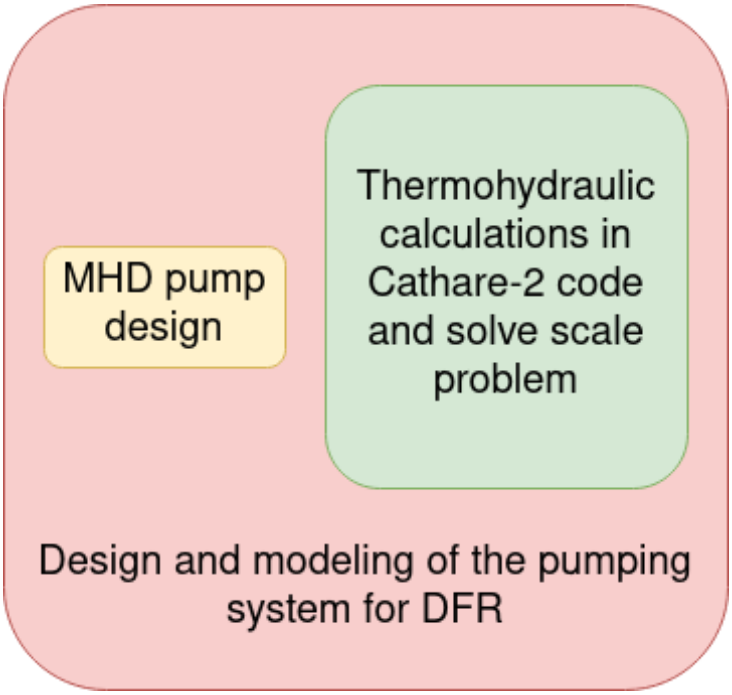

Figure 1.6: Diagram showing the common part of the presented results in the PhD thesis

Chapter 2

Theoretical background

The theoretical background is presented, starting first with a general topic such as DFR (section 2.1), then begin to describe more specific devices such as demonstrators (section 2.2) and finally magnetohydrodynamic pumps (section 2.6), preceded by a brief description of the physical phenomena with which they are associated, such as thermohydraulics (section 2.3), dimensionless numbers (section 2.4) and magnetohydrodynamics of liquid metals (section 2.5).

2.1 Dual Fluid Reactor

The Dual Fluid Reactor (DFR) is a fourth generation nuclear reactor. The novelty of this concept is the use of two circuits - one for the fuel, which will be molten salts or liquid metal, and one for the coolant, which will be liquid lead. The dual fluid reactor can be considered as a combination of other types of fourth-generation reactors - the MSR, LFR and SFR (figure 2.1) [Huke et al., 2015].

The DFR can be used in a variety of ways due to the temperature of the steam produced, which is around 1000 ^{o}C[Huke et al., 2015]. This reactor will have a large negative temperature coefficient, thus providing a much higher level of safety than common solutions used in the power industry. A schematic of the dual fluid reactor is shown in the figure 2.2 [Sierchuła et al., 2019].

There are two concepts of Dual Fluid Reactor in the literature regarding the working medium. In DFRs reactors, the fuel would be molten chloride or fluoride salts [Huke et al., 2015]. The second option is the DFRm, which would be based on a mixture

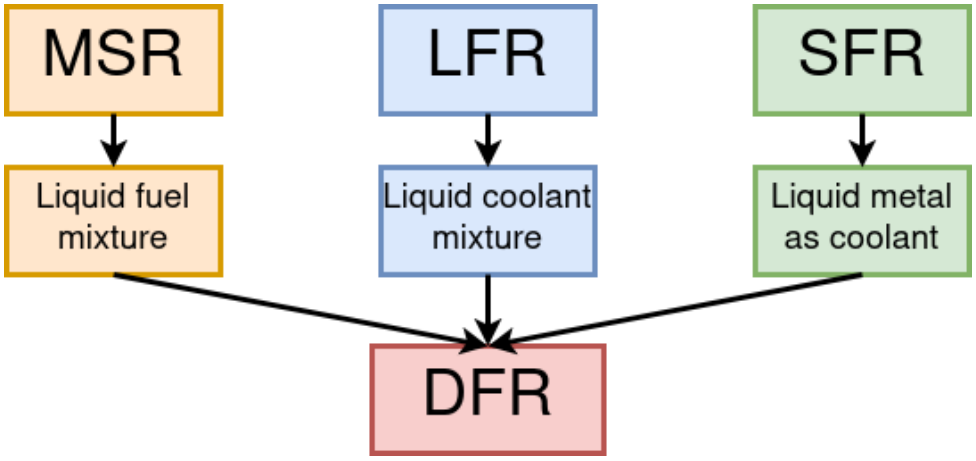

Figure 2.1: DFR idea scheme.

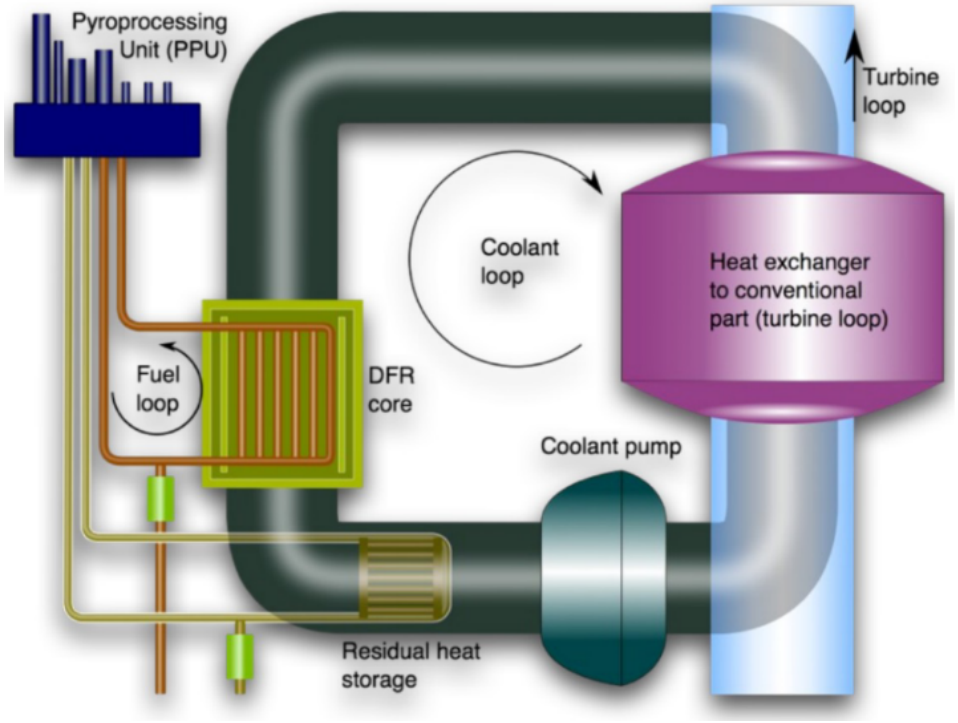

Figure 2.2: Dual fluid reactor concept [Huke et al., 2015].

of metallic chromium and uranium (so-called eutectic) [Sierchuła et al., 2019]. Liquid fuel circulation is a very important assumption for the design of this reactor, due to the possibility of removing fission products on the fly, and there will also be the possibility of controlling the flow rate, which translates into control of the energy produced in the reactor [Huke et al., 2015].

Another version of the DFR(pool-like reactor) being developed under the DFR patent [Huke et al., 2013] is the Hot Pipe Microreactor (HPR).

Heat pipe microreactor (HPR) is a type of nuclear reactor designed to be small,

portable and modular [Miao et al., 2023]. These reactors are typically designed for use in remote or off-grid locations where traditional power sources are not available.

A heat pipe micro-reactor is based on a heat pipe, which is a device capable of transferring heat from one place to another with the help of a working fluid. In the case of heat-pipe microreactors, the working fluid is usually a liquid metal, such as sodium or lithium, which is heated by nuclear fission reactions in the reactor core [Miao et al., 2023].

Heat pipes transfer heat to an energy conversion system, usually a turbine or a Stirling engine, that generates electricity. Using heat pipes allows for efficient heat transfer and can help increase the overall efficiency of the reactor.

Heat pipe microreactors are designed to be small and modular, with power outputs typically ranging from a few kilowatts to several megawatts [Miao et al., 2023]. This makes them ideal for use in remote locations or as backup power for critical infrastructure.

One of the advantages of heat pipe microreactors is their inherent safety. The small size and modular design allow the use of passive safety features, such as naturally circulating cooling and negative temperature response, which can help prevent accidents and reduce radiation risk. Collectively, heat pipe microreactors offer a promising new approach to small, portable, and safe nuclear power. Research and development is underway with a focus on improving the efficiency and reliability of these reactors, with the goal of making them a viable and sustainable energy source for the future [Wang et al., 2021a].

The difference between DFR and HPR is that in DFR we have fuel tubes submerged in the coolant pool, while in HPR, it is the other way around, as shown in the figure 2.3.

2.1.1 Reactor Safety

Liquid metal-based reactors, such as sodium-cooled fast reactors (SFR) and lead-cooled fast reactors (LFR), have unique safety features compared to conventional water-cooled reactors. While they offer some potential advantages, they also present some challenges that need to be carefully managed to ensure safe operation [Shaver and Wittenbrock, 1967], [Dunn and Wei, 1988].

The advantage of liquid metal coolants is their high boiling point, which reduces the risk of the coolant boiling and exposing the core of the reactor. In addition, liquid metal coolants are less likely to be activated by neutron beams, thus reducing the amount of radioactive waste generated.

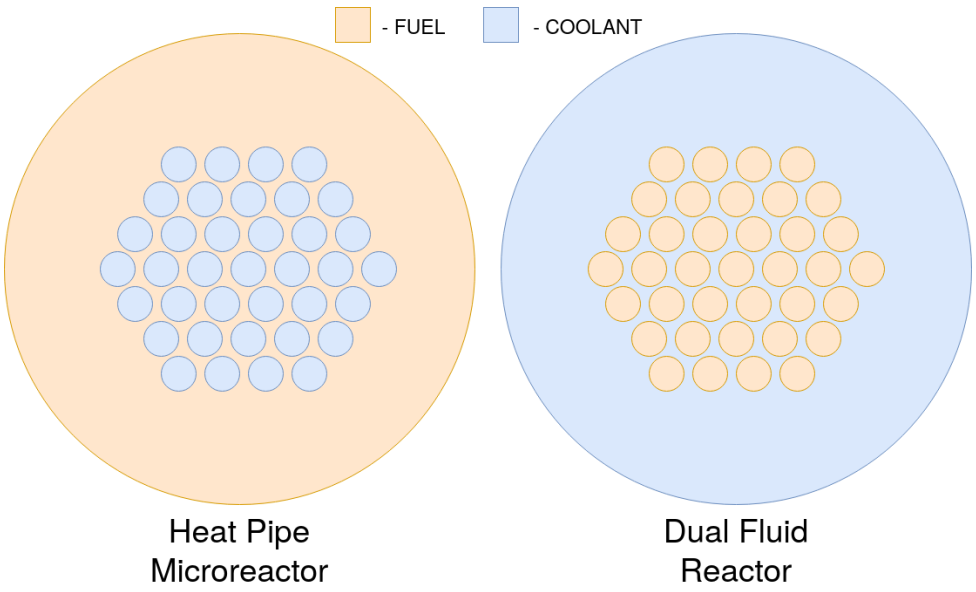

Figure 2.3: Simplified diagram comparing Heat Pipes Microreactor with Dual Fluid (pool-like) Reactor

However, liquid metal coolants also have some safety issues that need to be addressed. For example, they can ignite when exposed to air or water, leading to a loss of coolant accident. Additionally, liquid metal coolants can corrode some materials, so advanced materials must be used that can withstand high temperatures and chemical attack [Shaver and Wittenbrock, 1967],[Dunn and Wei, 1988].

To mitigate these safety challenges, liquid metal-based reactors are designed with multiple safety systems and redundant safety features. For example, SFRs and LFRs are designed with passive safety features such as natural recirculation cooling and negative temperature coefficients of reactivity to automatically shut down the reactor in the event of overheating.

Additionally, liquid metal-based reactors are typically designed with multiple physical barriers and containment structures to prevent the release of radioactive material in the event of an accident. These systems are carefully designed and tested to withstand the extreme conditions of potential accidents [Shaver and Wittenbrock, 1967], [Dunn and Wei, 1988].

Overall, liquid metal-based reactors can be designed to be safe and reliable, but require careful management and safety systems to ensure safe operation. Ongoing research and development is focused on improving the safety and reliability of these reactors with the goal of making them a viable and sustainable energy source of the future.

2.1.2 Liquid nuclear fuel

Neutronics is the study of the behavior and interactions of neutrons and matter, particularly as they relate to nuclear reactions and nuclear energy systems. It is the branch of nuclear engineering concerned with the design and analysis of nuclear reactors, nuclear fuel cycles, and other nuclear technologies [Thomas, 1999].

Neutron behavior is described by the Boltzmann transport equation, a partial differential equation that governs the neutron probability density function in phase space. The Boltzmann transport equation is given by

$$\frac{\delta\Psi(r,E,\Omega,t)}{\delta t} + \Omega\nabla\Psi(r,E,\Omega,t) + \sigma_t(r,E)\Psi(r,E,\Omega,t) = Q(r,E,\Omega,t) \qquad (2.1)$$

where Ψ, r, E, Ω, t, Σ_t and Q are respectively the neutron flux, spatial position, neutron energy, neutron orientation, time, total neutron cross section and the neutron source [Thomas, 1999].

Neutron flux is related to neutron density by the neutron diffusion equation.

Neutron diffusion equations are commonly used in reactor physics to model the behavior of neutrons in the core of a nuclear reactor can be solved numerically using various methods such as Finite difference method, finite element method, or Monte Carlo method.

Neutronics also includes the analysis of nuclear fuel behavior such as: fuel isotope depletion and radioisotope production. These processes are described by a system of coupled differential equations that describe the neutron flux, isotopic composition of the fuel, and various physical and chemical interactions between the fuel and coolant [Thomas, 1999].

In nuclear reactors, liquid metals have many advantages. As a coolant, they have a much higher conductivity than other materials, so they store heat much better and are used in high-temperature reactors. As fuel, on the other hand, they have a high energy density, while there is no radiation damage, and there is no risk of melting fuel rods and there is on-reprocessing possibility.

2.2 Demonstrators

Before designing and building a DFR with challenging operating parameters and very expensive construction materials, milestones called demonstrators are required. Demonstrators are devices designed to model the phenomena that can occur in a DFR reactor,

however the operating parameters are correspondingly lower and the size much smaller than the final DFR design. The single steps are named individually and are shown in the figure 2.4.

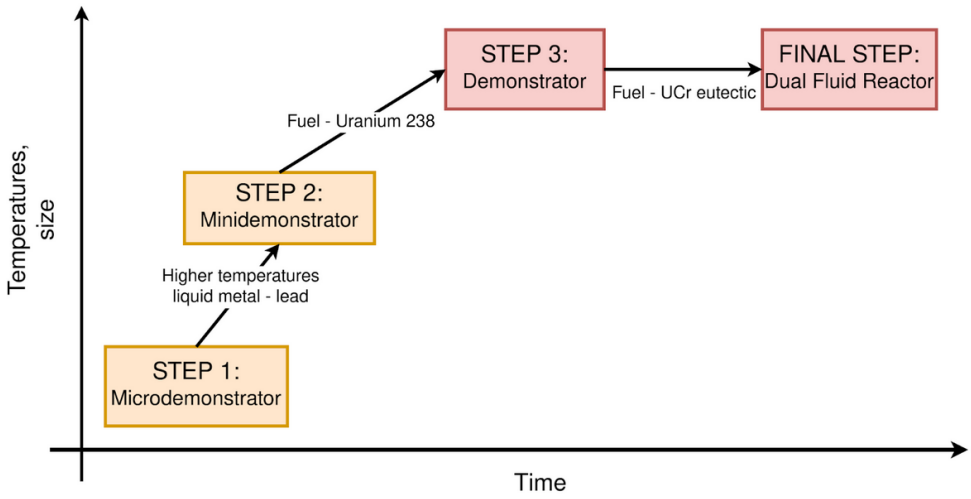

Figure 2.4: Steps from microdemonstrator to Dual Fluid reactor.

Step one, the construction that has the lowest temperature and size is the microdemonstrator (μDEMO). μDEMO is a device that consists of two loops - a fuel loop and a cooling loop. Both loops are filled with liquid metal, lead-bismuth eutectic. Figure 2.5 shows a simplified diagram of the μDEMO. The temperature range for which this device is to operate should not be more than 400 ^{o}C.

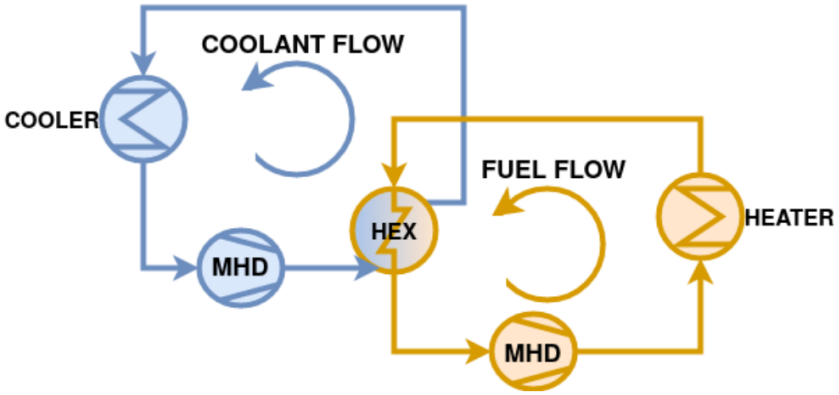

Figure 2.5: The simplified diagram of the μDEMO.

The next step will be a minidemonstrator mDEMO. This device will be similar in design to the μDEMO, however, the liquid lead will be used.

Table 2.1: Stages of DFR design

	Microdemonstrator	**Minidemonstrator**	**Demonstrator**	**DFR**
Fuel loop	lead-bismuth eutectic	lead	$U^{238}Cr$ eutectic	UCr eutectic
Coolant loop	lead-bismuth eutectic	lead	lead	lead
Temperatures	200 - 400 ^oC	1000 - 1200 ^oC	800 - 1300 ^oC	800 - 1300 ^oC

2.3 Thermal hydraulics

Thermal hydraulics is the study of the behavior of moving liquids, especially in their interaction with heat transfer processes. It is a branch of engineering concerned with the design and analysis of systems involving the transfer of energy through fluids.

One of the important equations in thermo-hydraulics is the Navier-Stokes equation (equation 2.2) [Friedlander, 2006], which describes the motion of fluids. It is given as:

$$\rho\left(\frac{\delta v}{\delta t}\right) = \nabla p + \mu\nabla^2 v + \rho g \tag{2.2}$$

where ρ, v, t, p μ, ∇, g, ∇^2 are the density of the liquid, velocity vector, time, pressure, dynamic viscosity of the liquid, the Nabla operator, acceleration due to gravity, and the Laplace operator.

In addition to the flow equations, such as the Navier-Stockes equations, an equation that includes heat transfer effects [Todreas and Kazimi, 2021]. The resulting equation is called the energy equation and is given by

$$\rho\left(\frac{\delta h}{\delta t}\right) = -\nabla(k\nabla T) + Q \tag{2.3}$$

where h is the specific enthalpy, T is the temperature, k is the thermal conductivity of the fluid, and Q is the heat transfer coefficient per unit volume.

The Navier-Stokes and energy equations form a set of simultaneous partial differential equations that describe the motion and energy transfer of fluids [Heywood, 2006]. These equations are used, among other things, in the design and analysis of various systems such as heat exchangers, boilers, and nuclear reactors [Todreas and Kazimi, 2021].

2.4 Dimensionless number

One of the hypotheses of the thesis is that on the basis of μDEMO, it is possible to predict the phenomena occurring in mDEMOand even in the final concept of DFR. To achieve this, it is necessary to consider which physical phenomena are of most important. One such phenomenon is the flow of liquid metal, while the other phenomenon that will be considered is the transfer of thermal energy between loops. To determine the similarity between the two systems, it was decided to use dimensionless numbers.

Dimensionless numbers are unitless coefficients, which are used to describe and compare physical systems [Lienhard and Lienhard, 2020]. If the coefficients for the two different models are identical, they can then be considered to be similar to each other. Due to the large number of dimensionless numbers, it was decided to limit the analysis to the four most commonly used in thermohydraulics and flow modeling.

Since there are a lot of dimensionless numbers, it was decided to choose the physical phenomena that are most interesting in demonstrators. Some of the types of phenomena chosen are flow phenomena: viscosity of fluids, interaction of internal forces Thermohydraulic phenomena were also selected: such as convection and thermal conductivity phenomena.

Reynolds number is a dimensionless number that describes the ratio of inertia forces to viscosity of a liquid metal. The Reynolds number is described by the equation 2.4:

$$Re = \frac{\rho v L}{\mu} \tag{2.4}$$

where L, μ, ρ and v are, respectively, the characteristic length, dynamic viscosity of the liquid metal,liquid metal density, and flow velocity.

The Reynolds number is used to determine the turbulence of a flow [Shashi Menon, 2015].

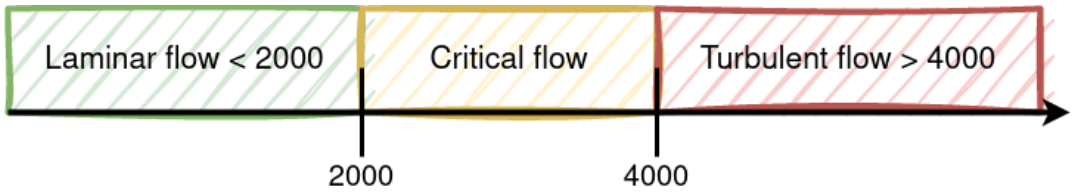

Figure 2.6: Range of flow turbulence type based on Reynolds number

Prandtl number is a dimensionless number that describes the ratio of viscosity diffusion rate to thermal diffusion rate. The relationship for the Prandtl number is shown in the

equation 2.5:

$$Pr = \frac{c_p \cdot \mu}{k} \tag{2.5}$$

where c_p, k are respectively the specific heat and thermal conductivity.

Figure 2.7 show that, this parameter is very strongly related to the material it describes - for example, for liquid metals the Prandtl number is very low (e.g., for sodium it is 0.01), while for air it is 0.72 and for water it is 6.90. The Prandtl number additionally shows whether the heat flow is more due to transport momentum or conductivity. For small values of the Prandtl number, thermal conductivity is more important than transport momentum (as is the case with liquid metals), while large values of the Prandtl number mean that transport momentum is more important than thermal conductivity (as is the case with water) [Rapp, 2017].

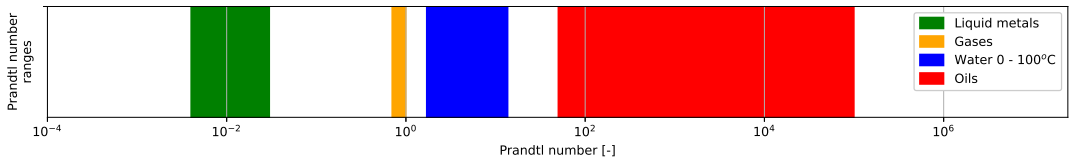

Figure 2.7: Prandtl ranges for different materials

The Nusselt number is a dimensionless number that describes the ratio of convective to conductive heat transfer.

$$Nu = \frac{h \cdot d}{k} \tag{2.6}$$

where h and d are, respectively, the coefficient of heat transfer coefficient and the characteristic linear dimension.

$$h = \frac{Fc}{\Delta T} \tag{2.7}$$

where Fc, ΔT are, respectively, Forced convection and difference temperatures between wall and liquid metal.

2.5 Liquid metal magnetohydrodynamics

Liquid metal magnetohydrodynamics (MHD) is the study of the behavior of liquid metals in the presence of electromagnetic fields. It is an interdisciplinary field that combines

the principles of fluid mechanics, electromagnetism, and materials science. Liquid metal MHD are particularly relevant to nuclear engineering where they are used for nuclear reactor design and analysis.

The motion of liquid metals, like classical fluid mechanics, is described by the Navier-Stokes equations 2.2 [Friedlander, 2006].

However, in the presence of electromagnetic fields, the Navier-Stokes equations are coupled to Maxwell's equations [Hampshire, 2018], which describe the behavior of electric and magnetic fields.

$$\begin{cases} \nabla \cdot E & = 4\pi\rho \\ \nabla \cdot B & = 0 \\ \nabla \times E & = -\frac{1}{c}\frac{\delta B}{\delta t} \\ \nabla \times B & = \frac{1}{c}\left(4\pi J + \frac{\delta E}{\delta t}\right) \end{cases} \tag{2.8}$$

The resulting equation is known as the MHD equation. This MHD equation for liquid metal is given by equations 2.9.

$$\begin{cases} \frac{\delta\rho}{\delta t} + \nabla(\rho v) & = 0 \\ \rho\left(\frac{\delta v}{\delta t} + v\nabla v\right) & = -\nabla p + \rho g + J \times B + \rho''\nabla^2 v \\ \frac{\delta B}{\delta t} & = \nabla \times (v \times B) + \rho''\nabla^2 B \\ \nabla B & = 0 \end{cases} \tag{2.9}$$

where J, B and ρ'' are respectively the current density, magnetic field, and the electrical liquid metal resistivity.

The first equation is the continuity equation representing conservation of mass. The second is a momentum equation that describes the conservation of momentum, including

the Lorentz force due to the interaction of current density and magnetic field. The third equation is the induction equation, which describes the conservation of magnetic flux, including the advection of the magnetic field by the velocity field and the diffusion of the magnetic field by the resistivity. The fourth equation is the condition of no magnetic field divergence.

Liquid metal MHDs are used in a variety of applications including liquid metal cooling systems in nuclear reactors, liquid metal batteries for energy storage, and metal casting processes for manufacturing. The complex and highly nonlinear behavior of liquid metals in MHD systems requires sophisticated modeling and simulation techniques to accurately predict and analyze.

2.6 Magnetohydrodynamic pumps

The history of magnetohydrodynamic (MHD) pump development began in the early 20th century with the discovery of the MHD effect. The first of this MHD pumps were demonstrated in 1950s, and by the 1960s research was sufficiently advanced to begin the development of his MHD pumps for practical applications. These pumps use a magnetic field to induce an electric current in a conductive fluid, creating a force that flow the fluid. MHD pumps have many advantages over conventional pumps, including: ability to operate without moving parts and to handle corrosive and radioactive liquids. However, due to high cost and technical challenges, MHD pumps have not yet been widely adopted. Ongoing research is focused on improving the efficiency and reliability of MHD pumps, which may become increasingly important in future applications such as nuclear power plants and space propulsion.

The solution to the high-temperature liquid metal flow problem appears to be a magnetohydrodynamic pump, which has no internal components ([Al-Habahbeh et al., 2016]) and the entire structure is outside the flow channel. MHD pumps can be divided into several groups that differ in the way the electromagnetic field is generated. In the literature, you can find various types of magnetohydrodynamic pumps. The list below shows a classification of the devices (figure 2.8).

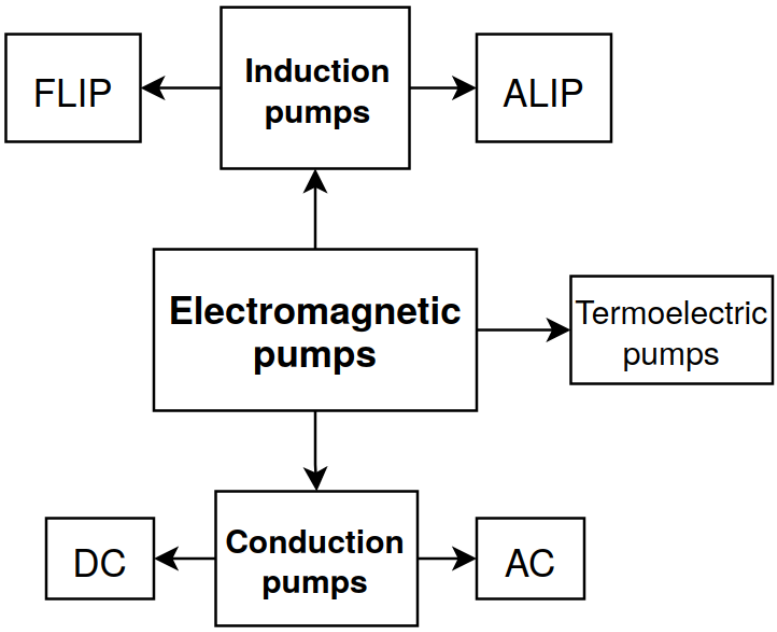

Figure 2.8: MHD pump classification diagrams

2.6.1 Induction pumps

The first group of magnetohydrodynamic pumps are induction pumps. The main feature of these devices is that they have no electrodes, and the current in the liquid is generated by a magnetic field. One of the best-known induction pumps, is the Flat Linear Induction Pump (FLIP). The magnetic field must be changed, so electromagnets are most often used. Figure 2.9 shows a simplified channel of a FLIP type induction pump.

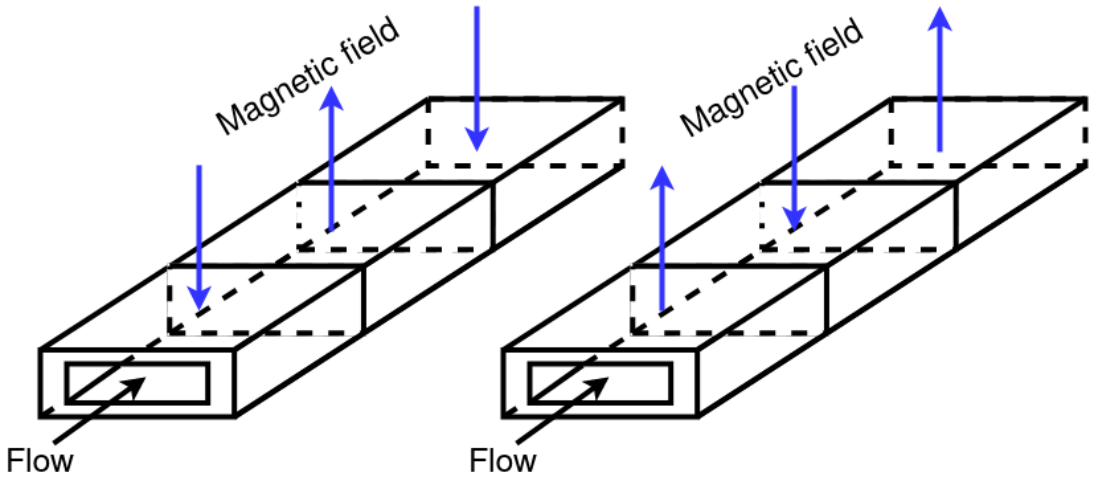

Figure 2.9: Induction MHD pump channel scheme

The advantage of such a pump is faster flow of the working fluid, but the flow is impulsive (which is due to the change in the direction of the magnetic field). An additional disadvantage of this solution is the more complicated design and mandatory cooling of electromagnets.

2.6.2 Conduction pumps

The second group includes conduction pumps, which supply current to the flowing medium by means of electrodes placed on the outer walls of the channel. These devices can be divided into direct current (DC) and alternating current (AC) induction pumps. The second group of pumps are induction pumps in which the current is induced in the flowing medium as a result of magnetic field interaction.

The most important advantages of DC conduction pumps are ease of understanding the principle of operation of such a device and uncomplicated design. This enables easier mathematical description for pumps modeling.

An additional advantage is that it does not have mechanically moving or rotating parts in its flow channel, so the device has a lower failure rate. In addition, the pump can be used in structures where access is difficult and repair would be impossible [Polzin, 2007].

Figure 2.10 shows the conduction channel scheme of a DC magnetohydrodynamic pump. W_d, H_d, L and d are the width, height, length and wall thickness of the pump channel, respectively. On the other hand, the depicted arrows represent direction of the magnetic (B) and electric (I) fields. The blue colour indicates the location of the magnets and the orange colour indicates the location of the electrodes.

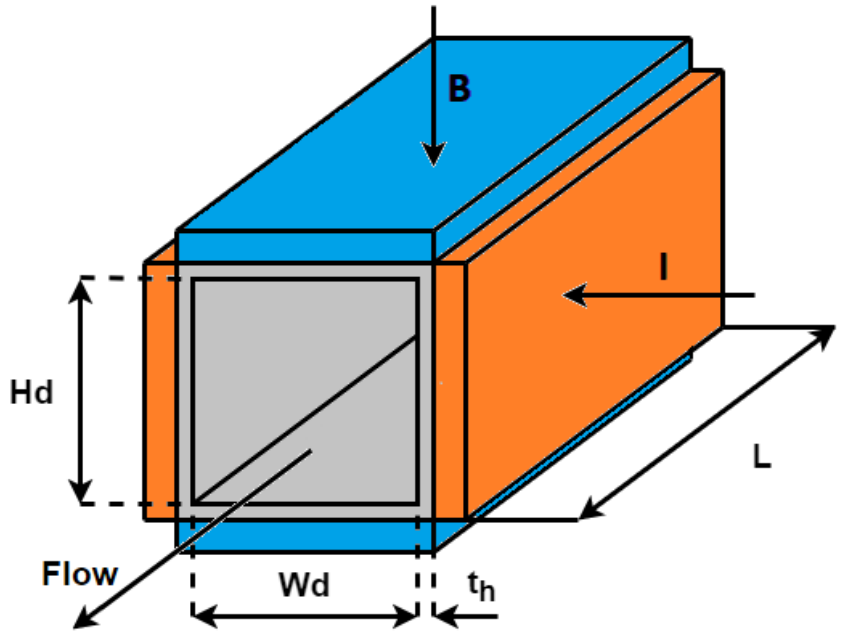

Figure 2.10: Conduction MHD pump channel scheme

Part II

Tools

Chapter 3

Calculation tools

The chapter describes the software and all the mathematical tools used in the work.

Because the research problems in this thesis are very complicated, specialized mathematical tools and models had to be used. For the thermohydraulic part of the single-phase flow (subsection 3.1), specialized software - Cathare-2 was used, which is described in more detail in subsection (subsection 3.2). For the magnetohydrodynamic calculations, since no suitable software is available, a program was written to solve the inverse Equivalent Circuit Method problem (subsection 3.3) and specialized optimization scripts such as simulation annealing, polynomial approximation and multi-element regression), which are described in sections (subsections subsection 4.1 - 4.2).

3.1 Single phase flow

Single-phase flow is the flow of a single liquid phase, such as a liquid or gas, through a conduit or porous medium [Todreas and Kazimi, 2021]. It is a fundamental concept in fluid mechanics and is used in a wide variety of engineering applications, including the design and analysis of piping, heat exchangers, and chemical reactors.

Single-phase flow behavior is described by the Navier-Stokes equations, a set of partial differential equations that describe the conservation of mass, momentum, and energy in a fluid [Friedlander, 2006]. All of this equations for single-phase flow is given by

$$\begin{cases} \frac{\delta\rho}{\delta t} + \nabla(\rho v) & = 0 \\ \rho\left(\frac{\delta v}{\delta t} + v\nabla v\right) & = -\nabla p + \mu\nabla^2 v \\ \rho C_p\left(\frac{\delta T}{\delta t} + v\nabla T\right) & = \nabla(k\nabla T) + Q \end{cases} \tag{3.1}$$

where ρ is the density of the fluid, v is the velocity vector, t is time, p is the pressure, μ is the kinematic viscosity, C_p is the specific heat at constant pressure, T is the temperature, k is the thermal conductivity, and Q is the heat source or sink.

The first equation is the continuity equation representing conservation of mass. The second equation is a momentum equation that describes conservation of momentum, including viscous stresses due to the viscosity of the fluid. The third equation is the energy equation, which describes the conservation of energy, including the conduction of heat through fluids and the generation or absorption of heat by chemical reactions or other sources [Friedlander, 2006].

These equations are highly nonlinear and difficult to solve analytically except in simple cases. So in practice we solve them using numerical methods such as finite difference method, finite element method and finite volume method. These methods discretize the equations into a set of algebraic equations that can be solved using iterative techniques such as Gauss-Seidel and conjugate gradient methods. Single-phase flow is characterized by various parameters such as Reynolds number, Prandtl number and Nusselt number. These parameters depend on the physical properties of the fluid, flow geometry, and boundary conditions. These parameters are used to classify and analyze different types of flows such as laminar and turbulent and predict their behavior under different operating conditions [Friedlander, 2006].

3.2 Cathare-2 software

CATHARE [Geffraye et al., 2011] (Code for Analysis of THermalhydraulics during an Accident of Reactor and safety Evaluation) is a two-phase thermal-hydraulic software developed since 1979 at CEA-Grenoble under an agreement between CEA, EDF, AREVA

and IRSN. This code is based on a two-phase model with six equations (conservation of mass, moments and energy for both phases). This simulator has a modular structure and can operate in 0D, 1D or 3D and is capable of modeling any type of reactor. This means that it is suitable software for performing calculations for nuclear reactors [Geffraye et al., 2011]. Moreover, Cathare-2 has, by default, liquid metals as working media in addition to water, which is essential for minidemonstrator and microdemonstrator design and modeling.

Before the calculations were made, a literature review was performed for the application of the Cathare-2 code to liquid metals.

In the article [Polidori and Kadri, 2012], calculations were made for liquid metal - lead bismuth eutectic. In the other articles ([Anderhuber et al., 2015], [Alpy et al., 2016], [Bubelis et al., 2017]), calculations were made for liquid sodium.

Analyzing the [Polidori, 2010] report, it can be found out that Cathare-2 was additionally developed to perform calculations for liquid metals. The Cathare-HLM (HLM - High temperature Liquid Metal) is a fork from the Cathare-2 code source code version 2.5_2. It was developed for its ability to perform calculations for high-temperature liquid metals. The authors focused mainly on liquid lead and on lead-bismuth eutectic. The Cathare-HLM code was then merged with the main Cathare-2 code in version 2.5_3.

The Cathare code was tested for liquid sodium. First, it was validated on GR19 Sodium boiling experiments [Anderhuber et al., 2015], then the Cathare-2 results were compared with the SABENA code [Alpy et al., 2016]. The last application of Cathare-2 for liquid metal, was calculations for ASTRID like reactor [Bubelis et al., 2017].

Figure 3.1 shows a simplified history of the development of Cathare-2, reconstructed from [Geffraye et al., 2011] and [Polidori, 2010]. As can be seen, since 2009, the ability to perform calculations for liquid sodium has been implemented, while in 2013, after Cathare-2 was merged with Cathare-HLM, calculations can also be performed for liquid lead, which is the working medium for the mDEMO, and for lead-bismuth eutectic, which is the working medium for the μDEMO.

In this work, the latest version of Cathare-2 version 25_3mod9.1 created in 2019 was used for calculations.

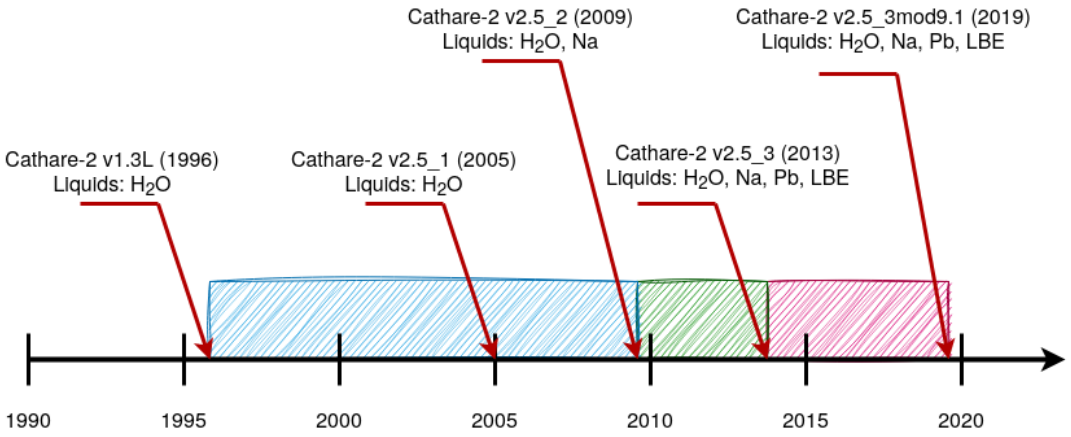

Figure 3.1: Cathare2 version releases

3.3 Equivalent Circuit Methods

MHD pumps modeling is a complex issue, therefore, appropriate mathematical methods had to be used. The most important task is to solve the MHD equations, which are a combination of Navier-Stokes equations and Maxwell's equations. Different computational methods — numerical and analytical — are used in the literature. Numerical methods usually use the Finite Element Method or the Finite Volume Method. Analytical methods, on the other hand, use various models, simplifications, or transformations of formulas. An example of such simplification is the Equivalent Circuit Method (ECM) [Lee and Kim, 2017]. This method is characterized by the fact that complex MHD equations are replaced by an electrical system of resistors and sources of electromotive force [Borges et al., 2003], [Borges et al., 2010], [Borges et al., 2007], [Lee and Kim, 2017]. The ECM was proposed by [Watt, 1959] who used a simple electrical system as a model for a DC MHD pump. [Borges et al., 2003] refined the model by deriving the final equation for the pressure produced by the MHD pump, which the author used in his BEMC-1 program. Subsequently [Lee and Kim, 2017] made changes in the form of the equations for the equivalent resistances and added a term related to hydrodynamic losses in the channel of the MHD pump to the formula for the generated pressure.

Figure 3.3 [Lee and Kim, 2017] shows a schematic of the balanced electrical circuit of a DC MHD pump that is modelled by the ECM. The current has two possibilities to flow - either across the liquid metal or across the walls of the pump channel (figure 3.2).

The resistances R_{LM}, R_w and R_b are described in the formulas 3.8 - 3.10 and will be discussed further in the text. The resistance R_0 is the resistance of the conductor

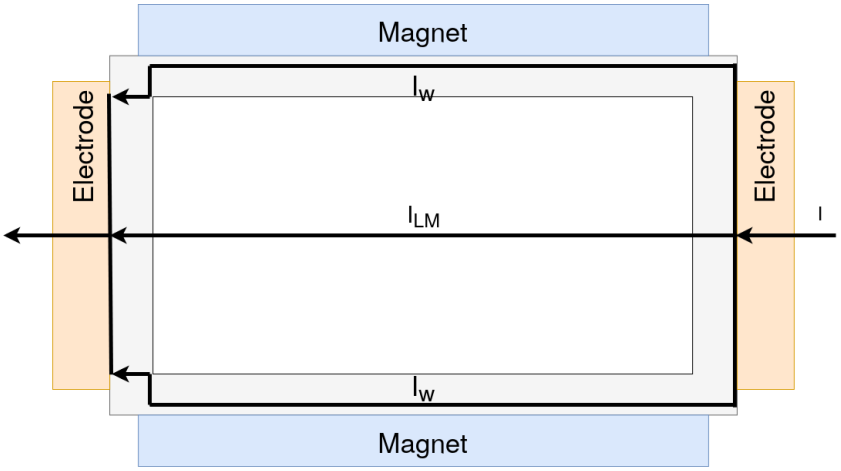

Figure 3.2: Diagram showing the current flow in the MHD pump.

wires supplying current to the MHD pump, so it will not be considered further in the calculations. The electromotive force E simulates the losses due to the flow of liquid metal in a magnetic field:

$$E = \frac{B_m Q}{H_d} \tag{3.2}$$

Where B_m, H_d and Q are the magnetic induction, pump channel height and flow rate, respectively.

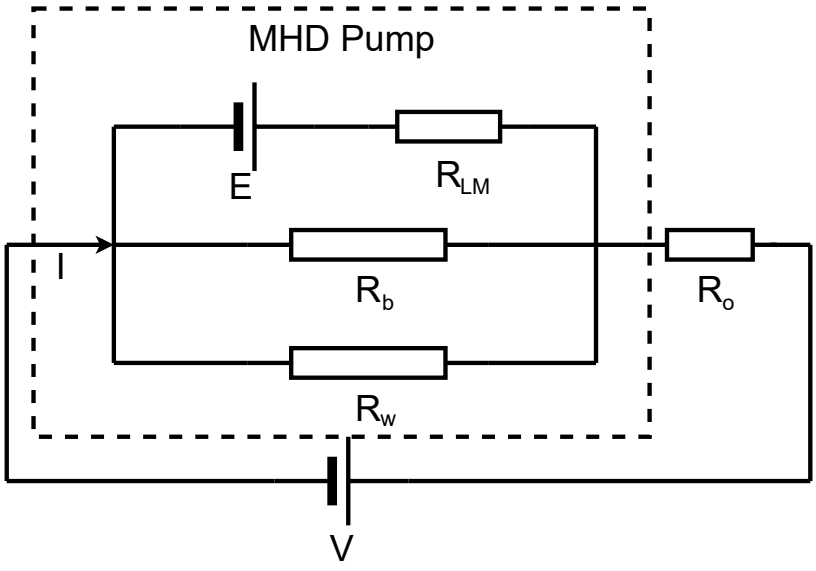

Figure 3.3: Schematic of the balanced electrical circuit of a DC MHD pump

After applying the ECM equations, the following formula is obtained:

$$\frac{f_d\ \rho_{(LM)}\ L_L(W_d+H_d)}{4(W_dH_d)^3}Q^2 = \frac{B_mI_1R_{ver}}{(R_{ver}+R_{LM})H_d^2} - \frac{B_m^2Q}{(R_{ver}+R_{LM})H_d^2} - \\ - \frac{f_d\ \rho_{(LM)}\ L_PQ^2(W_d+H_d)}{4(W_dH_d)^3}, \tag{3.3}$$

where, $\rho_{(LM)}$, f_d, I_1, L, R_{LM}, and R_{ver} are the liquid metal density, flow resistance factor, input current to the MHD pump, pump channel length, resistance, and equivalent resistance, respectively. The relationship 3.3 can be divided into four parts. The first term on the left hand side of the equation represents the pressure loss measured in the circuit (ΔP). The first term on the right hand side of the equation represents the pressure generated by the pump due to the magnetic field (ΔP_w). The second term corresponds to the electromagnetic pressure losses (ΔP_e) and The last term is the hydrodynamic loss along the pump channel (ΔP_h).

To simplify the formulas, the following coefficients were introduced:

The coefficient A corresponds to the pressure losses in the pump channel or throughout the simplified loop [Lee and Kim, 2017], [Borges et al., 2007].

$$A = \frac{f_d\ \rho_{(LM)}\ (W_d+H_d)}{4(W_dH_d)^3}. \tag{3.4}$$

The coefficient B corresponds to the electrical losses in a MHD pump,

$$B = \frac{B_m^2}{(R_{ver}+R_{LM})H_d^2}. \tag{3.5}$$

The coefficient C corresponds to the pressure generated by the pump,

$$C = \frac{B_mR_{ver}}{(R_{ver}+R_{LM})H_d^2}. \tag{3.6}$$

On the other hand R_{ver} is the equivalent resistance, which is calculated by the relationship shown in the equation 3.7.

$$R_{ver} = \frac{R_w \cdot R_b}{R_w + R_b}, \tag{3.7}$$

where R_b and R_w are the equivalent resistance corresponding to the frozen field and the equivalent resistance associated with the pump channel walls, respectively.

The resistance R_{LM} corresponds to the electrical losses in the liquid metal and is expressed by the formula:

$$R_{LM} = \frac{\rho'_{LM}W_d}{H_dL}, \tag{3.8}$$

where ρ'_{LM} is the resistivity of the liquid metal.

The resistance R_w corresponds to the electrical losses on the pump walls, so it depends on the resistivity of the pump material and the thickness of the pump channel walls.

$$R_w = \frac{\rho'_w W_d}{2dL}, \tag{3.9}$$

where ρ'_w and d are the resistivity of the pump channel walls and the width of the pump channel, respectively.

In the relation for the resistivity R_b (Eq. 3.10) there is a "fringe factor" resulting from the existence of the so-called frozen field that moves along with the liquid metal. The value of this factor is from [Lee and Kim, 2017].

$$R_b = \frac{\rho'_{LM}}{K_2 H_d} \tag{3.10}$$

where K_2 is the "fringe factor".

Equations 3.3 - 3.10 were taken directly from [Lee and Kim, 2017].

For such coefficients, the relation for 3.3 takes the following form:

$$AL_{loop}Q^2 = CI - BQ - AL_{pump}Q^2, \tag{3.11}$$

which can be transformed into pressure terms:

$$\Delta P_{loop,loss} = \Delta P_{pump,gain} - \Delta P_{EM,loss} - \Delta P_{pump,loss} \tag{3.12}$$

and after rearranging:

$$\Delta P_{pump,gain} = \Delta P_{loop,loss} + \Delta P_{EM,loss} + \Delta P_{pump,loss}. \tag{3.13}$$

The pressure generated by the pump due to the magnetic field (ΔP_w) is expressed by the formula:

$$\Delta P_w = \Delta P_{pump,gain} = CI_1 \tag{3.14}$$

The electromagnetic pressure losses (ΔP_e) is expressed by the formula:

$$\Delta P_e = \Delta P_{EM,loss} = BQ \tag{3.15}$$

The hydrodynamic loss along the pump channel (ΔP_h) is expressed by the formula:

$$\Delta P_h = \Delta P_{pump,loss} = AQ^2 \tag{3.16}$$

Q is the flow rate, which is calculated from the following relationship:

$$Q = vW_dH_d \tag{3.17}$$

where v is the velocity of the moving flowing medium.

In works by [Borges et al., 2010] and [Lee and Kim, 2017] the authors use the ECM to calculate the total pressure produced by a DC MHD pump. However, since the pressure produced by the pump is equal to the pressure drop across the fuel loop, the calculation can be reversed to obtain the input current to the MHD pump from the given pressure drop.

The goal of this paper is to design a MHD pump and optimize its geometry by achieving the minimum current value. This solution is very advantageous for design and economic reasons. The biggest drawback of magnetohydrodynamic pumps is their power supply. Usually one needs a source that produces high current and low voltage, and such designs are very expensive to build. By minimizing the current, the cost of designing and manufacturing such a power supply is significantly reduced.

Due to the fact that calculation were performed under assumption of constant pressure difference and constant pump channel cross section, the Lorentz force is also constant, as shown in eq. 3.18.

$$\Delta P_{pump,loss} = \frac{F}{A_d} = \frac{B \cdot I_{ECM} \cdot W_d}{W_d H_d} \tag{3.18}$$

where F and I_{ECM} are Lorentz force and total ECM current.

Chapter 4

Optimization and regression tools

4.1 Meta-heuristic algorithms

An optimization problem is a computational problem in which the globally best solution (global maximum or global minimum) must be found in a given constrained space of optimized parameters. Searching every point in it would be very time consuming and would require a lot of computational power. One method that can be used to speed up this process is metaheuristic algorithms. They are based on a random search of the space in order to obtain a fast but not necessarily perfect solution to the problem. In these algorithms, the accuracy of the results must be reconciled with the computation time. The faster the result obtained, the greater the difference between the obtained value and the true solution.

4.1.1 Simulated Annealing

It was decided to use the simulation annealing method [Kirkpatrick et al., 1983], [Černý, 1985] to optimize the pump geometry. This method is analogous to the phenomenon of crystal ordering during temperature reduction. The structure of solids is not ordered for high temperatures.

The ordering occurs as the material is cooled [Kirkpatrick et al., 1983] [Černý, 1985]. The entire algorithm that was used to find the optimal pump geometry is based on this assumption.

While solving the optimization problem, there is a possibility that a local minimum will be found and accepted as a final result. To avoid this, the simulated annealing

algorithm can accepts unwanted results with some probability. This probability decreases as the algorithm is running, which ensures that it does not terminate the computation at the local minimum.

The principle of the algorithm is shown in Figure 4.1.

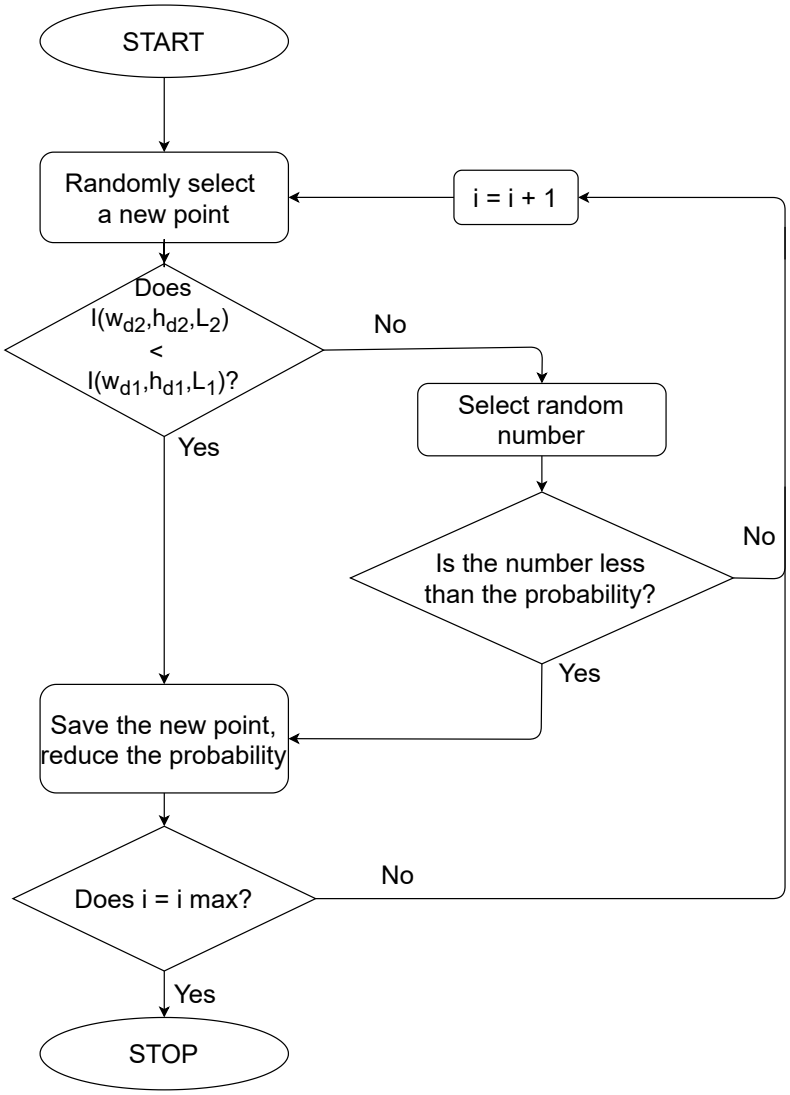

Figure 4.1: Scheme of the Simulated Annealing algorithm.

After the user provides a start variable, the algorithm randomly selects a point that is less than or equal to a step from the start point. Then the values of the function are compared and if the newly generated point has a better (smaller if the search is for a minimum or larger when searching for a maximum) value than the starting point, then it is accepted and the algorithm is executed again to search for another point to compare.

However, if the result is worse, then there is a probability that it will be accepted. The algorithm draws a number from 0 to 1. If this number is less than the probability value, then the result is accepted, otherwise the result is rejected. This probability, like the temperature when cooling the crystals, is reduced with each iteration. Application of this method reduces the risk that a local solution is found instead of a global solution [Kirkpatrick et al., 1983] [Černý, 1985] [Laarhoven and Aarts, 1987].

4.2 Multivariate regression

Multivariate regression is a statistical technique used to model the relationship between multiple independent variables and a single dependent variable. This is an extension of simple linear regression that considers only one independent variable.

The goal of multivariate regression is to identify a linear relationship between a dependent variable and some independent variables. Regression models estimate the values of coefficients that define the relationships between variables. These coefficients represent the expected change in the dependent variable for each unit change in each independent variable while keeping all other variables constant.

Multivariate regression is used for various purposes, such as predicting the value of a dependent variable based on the values of an independent variable, assessing the effect of an independent variable on a dependent variable, and identifying important independent variables that influence a dependent influence variable. can be used for . Common types of multivariate regression include multiple linear regression, polynomial regression, and logistic regression. Multivariate regression is widely used in fields such as economics, social sciences, engineering, and biology.

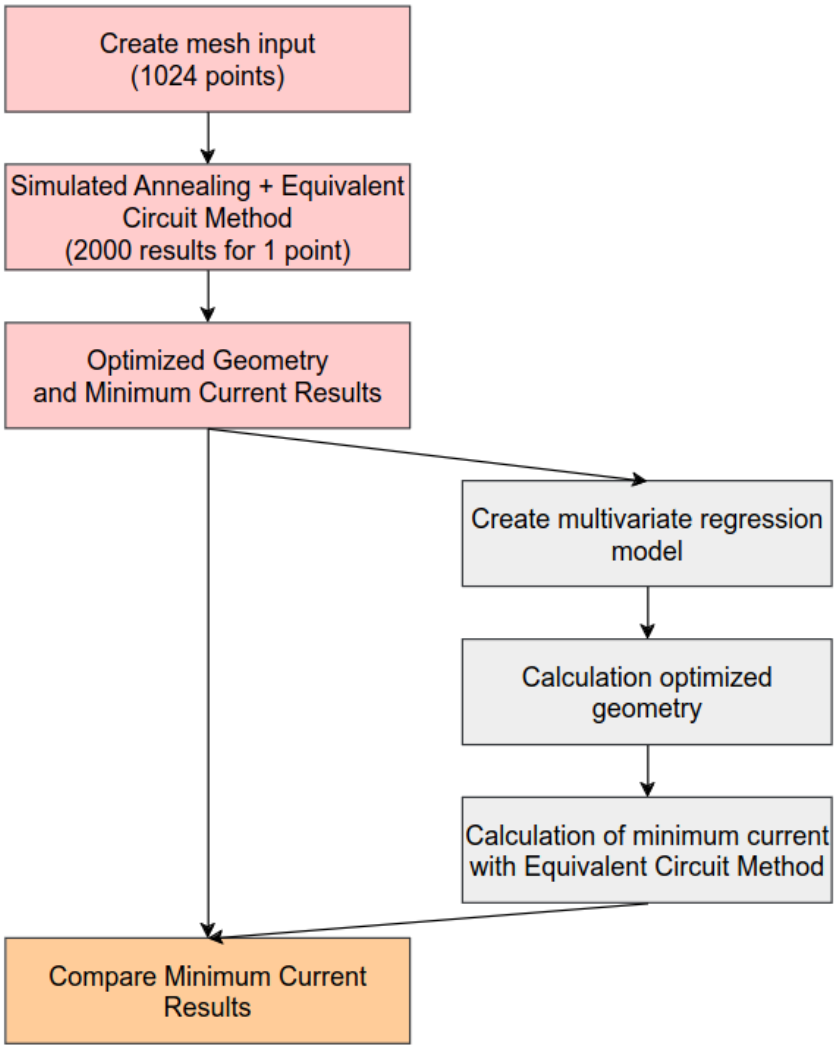

Figure 4.2: Scheme of the Multivariate Regression algorithm.

Part III

Results and conclusions

Chapter 5

Demonstrators hydraulic calculations

DFR(m) is a new concept of nuclear reactor, so simplified models of this design should be established at the beginning so that proper tests and experiments can be conducted under safe, and controlled conditions. One such test system has been named the minidemonstrator and its purpose will be to perform thermal-fluid experiments.

The purpose of the work was to select appropriate dimensionless numbers, with which to compare demonstrators among themselves. This solution would allow, based on the data from the microdemonstrator, predict the operating parameters for the minidemonstrator and then for the conceptual DFR reactor.

The figure 5.1 shows the calculation scheme for μDEMO and mDEMO.

In the section 5.1, the models in Cathare-2 software for μDEMO and mDEMOare presented. Next, the following sections present the results of the calculations - the subsection 5.2.1 presents an analysis of the results for the matched Nusselt number, while the subsection 5.2.2 presents an analysis of how flow velocity affects heat transfer in the two demonstrators.

5.1 Cathare-2 models

Demonstrator models made in Cathare-2 software are similar to each other; however, they differ in working factors. Because liquid metals have different parameters, such as density or dynamic viscosity, the dimensionless numbers will differ. To prevent this, the core geometry (i.e., the diameter and length of the core tubes, for example) would have to be transformed accordingly. Therefore, two similarity coefficients were introduced: the

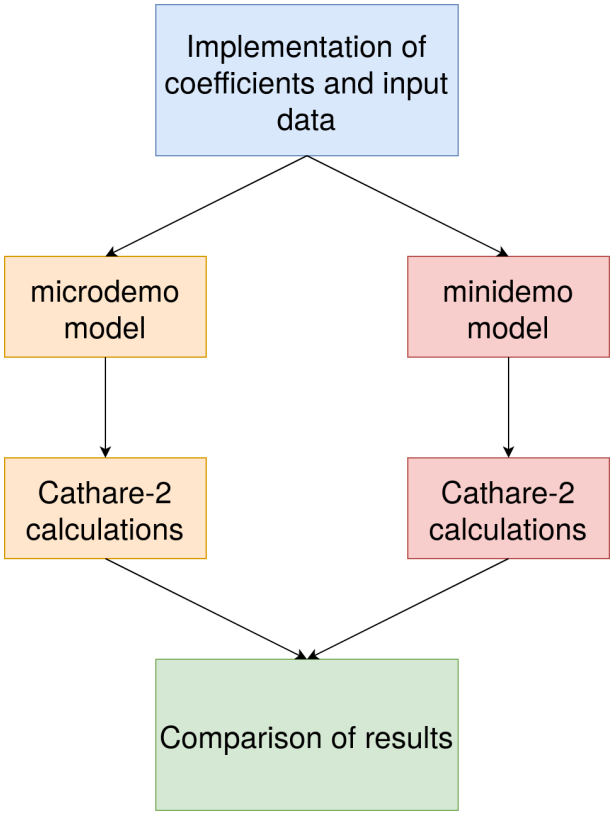

Figure 5.1: The calculation scheme for μDEMO and mDEMO

similarity coefficient of the width of the core tubes Re_A, and the similarity coefficient of the core height Eu_A.

By controlling the coefficient Re_A, either the Reynolds number or the Nusselt number can be adjusted (There is no possibility to adjust the diameters so that the two numbers are similar in both demonstrators).

Before calculations for demonstrators can be performed, the validity of the Cathare-2 software results for liquid metals must be tested. This code was written to simulate water reactors and has recently been used for gas cooled reactors.

The article ([Anderhuber et al., 2015]) performed a validation of the Cathare-2 code with a liquid sodium loop experiment. The results have been satisfactory. On the other side, the ENEA's cooperation with the CEA resulted in an improved code - Cathare-HLM ([Polidori et al., 2012]).

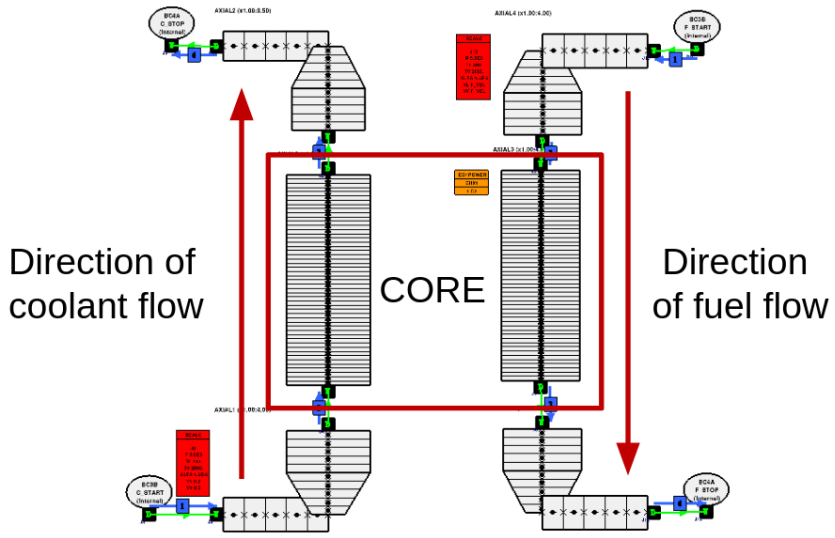

Figure 5.2: μDEMO and mDEMO diagram made in Cathare-2 software.

5.2 Comparison of water and liquid metal properties for a μDEMO

First, a calculation was made for the model to see the differences between using water and liquid metal. The main differences between the liquids are the melting point and boiling point of both materials. For standard pressure, water melts at 0 ^{o}C, while boiling at 100 ^{o}C, while for lead-bismuth these temperatures are respectively: melting point 123.5 ^{o}C, boiling point 1670 ^{o}C, and for pure lead: melting point 327.46 ^{o}C, boiling point 1746 ^{o}C. Such high boiling points for liquid metals are ideal for use in DFR, which is expected to reach a maximum temperature of 1300 ^{o}C.

Table 5.1: Comparison of fluid states for temperatures that can occur in the DFR.

Temperatures	Water	Lead-bismuth	Pure Lead
Water boiling temperature (100 ^{o}C)	Gas	Solid	Solid
Lead-bismuth eutectic melting temperature (123.5 ^{o}C)	Gas	Liquid	Solid
The highest μDEMO temperature (400 ^{o}C)	Impossible	Liquid	Liquid
The lowest DFR temperature (800 ^{o}C)	Impossible	Liquid	Liquid
The highest DFRtemperature (1400 ^{o}C)	Impossible	Liquid	Liquid

5.2.1 Scale problem for liquids metal

The first task that had to be done was to find the parameters for which the Reynolds number for both demonstrators would be the same. The formula for the Reynolds number is as follows:

$$Re = \frac{\rho v D}{\mu} \tag{5.1}$$

Where ρ, v, D, and μ are the liquid metal density, flow velocity, characteristic length, and dynamic viscosity of the liquid metal, respectively.

Considering that density and viscosity are material parameters, therefore the only values that can be manually controlled are velocity and characteristic length.

The table below shows the parameters for which similar Reynolds numbers were achieved:

	Microdemonstrator	Minidemonstrator
Velocity range $\left[\frac{m}{s}\right]$	0.34 - 2.72	0.1 - 0.8
Pipe diameter [m]	0.0698	0.0465
Pipe height [m]	0.5	0.5

Analyzing the table, it can be seen that for μDEMO, we have to use a larger diameter by 1.5, and higher velocities by 3.4, to get the same Reynolds number. This means that we need to increase the flow rate by as much as 2.25 times.

Then, the relative error between the demonstrators' results was calculated to be able to compare the differences between different Reynolds number values. The following equation was used to determine the relative error:

$$\delta = \frac{|Re^{\mu} - Re^{m}|}{Re^{\mu}} \cdot 100\% \tag{5.2}$$

Results showing relative errors for Reynolds numbers are shown in figure 5.4. As can be seen, for lower velocities these errors are larger than for higher velocities. For higher velocities, the relative error does not exceed 3 %.

In the next step, the parameters of the demonstrators were adjusted to match the Nusselt numbers with each other. Since the working medium is liquid metals, the following relationship had to be used to determine the Nusselt number:

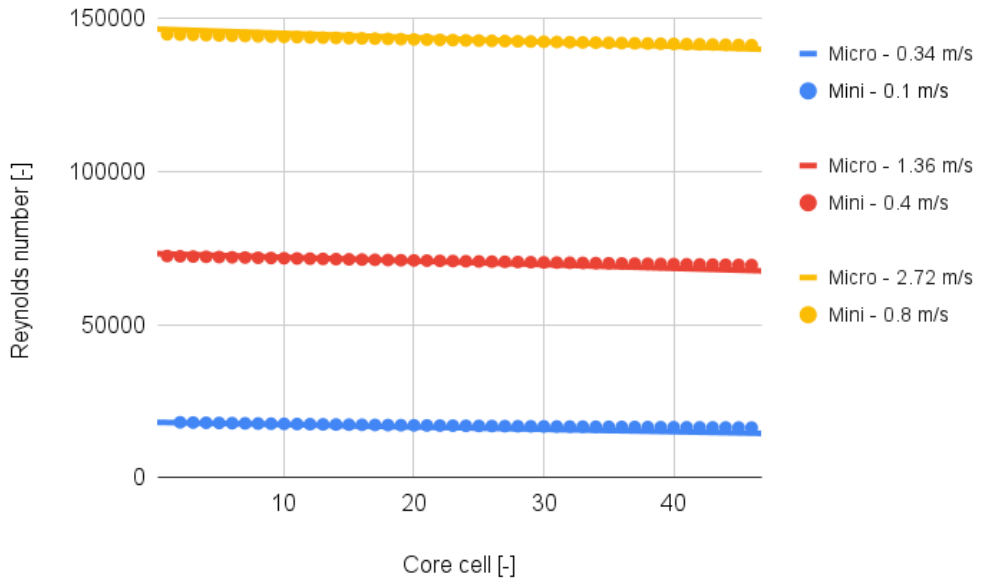

Figure 5.3: Results for μDEMO and mDEMO with similarity of Reynolds numbers

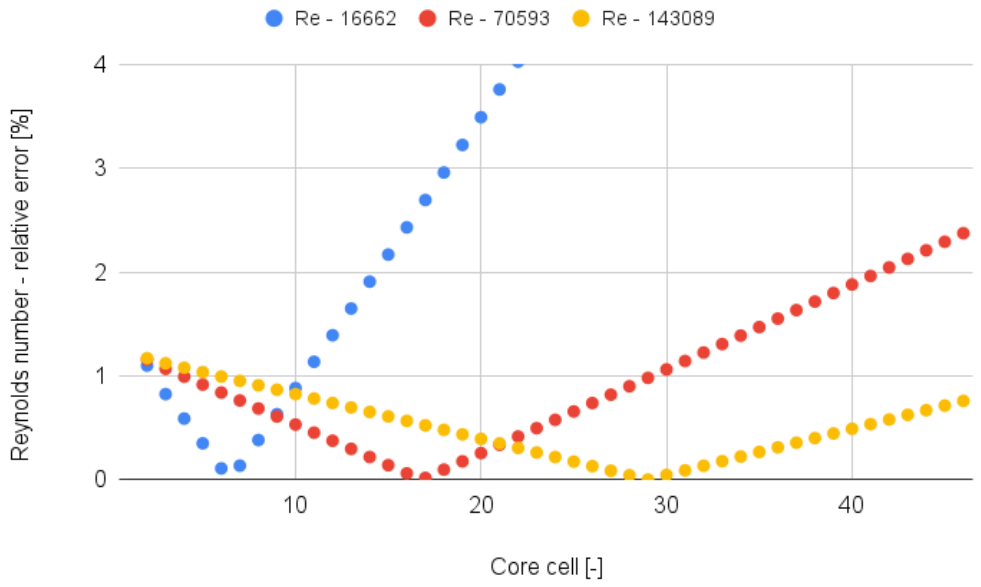

Figure 5.4: Relative errors of Reynolds number for μDEMOand mDEMO.

$$Nu = \frac{h \cdot d}{k} \tag{5.3}$$

Where h, d and k are the thermal conductivity coefficient, characteristic linear dimension, respectively and the heat transfer coefficient.

As with the Reynolds number, the parameters that can be manually varied are the liquid metal velocity and the characteristic linear dimension.

	Microdemonstrator	Minidemonstrator
Velocity range $\left[\frac{m}{s}\right]$	0.1 - 0.8	0.1 - 0.8
Pipe diameter [m]	0.0279	0.0465
Pipe height [m]	0.5	0.5

analyzing the table, you can see that for μDEMO we need to use a smaller diameter by 0.6, and the velocities should stay the same as for μDEMO to get the same Nusselt number. This means that we need to reduce the flow rate by as much as 0.36 times.

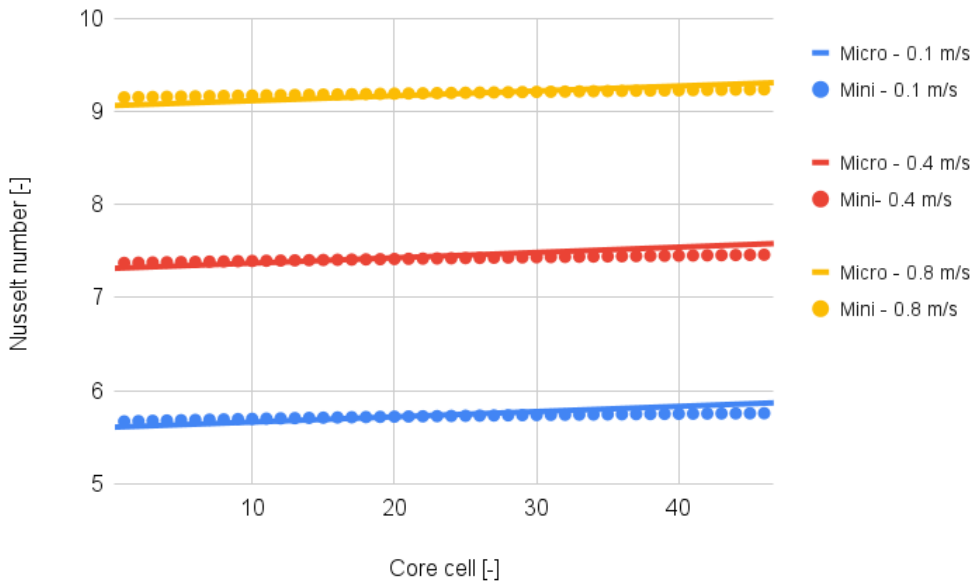

Then, the relative error between the demonstrators' results was calculated to be able to compare the differences between different Nusselt number values. The following equation was used to determine the relative error:

$$\delta = \frac{|Nu^{\mu} - Nu^{m}|}{Nu^{\mu}} \cdot 100\% \tag{5.4}$$

Results showing relative errors for Reynolds numbers are shown in figure 5.5. The relative error for all velocities does not exceed 2 %.

$$Nu^{\mu} \approx Nu^{m} \tag{5.5}$$
$$\frac{h^{\mu}d^{\mu}}{k^{\mu}} = \frac{h^{m}d^{m}}{k^{m}}$$

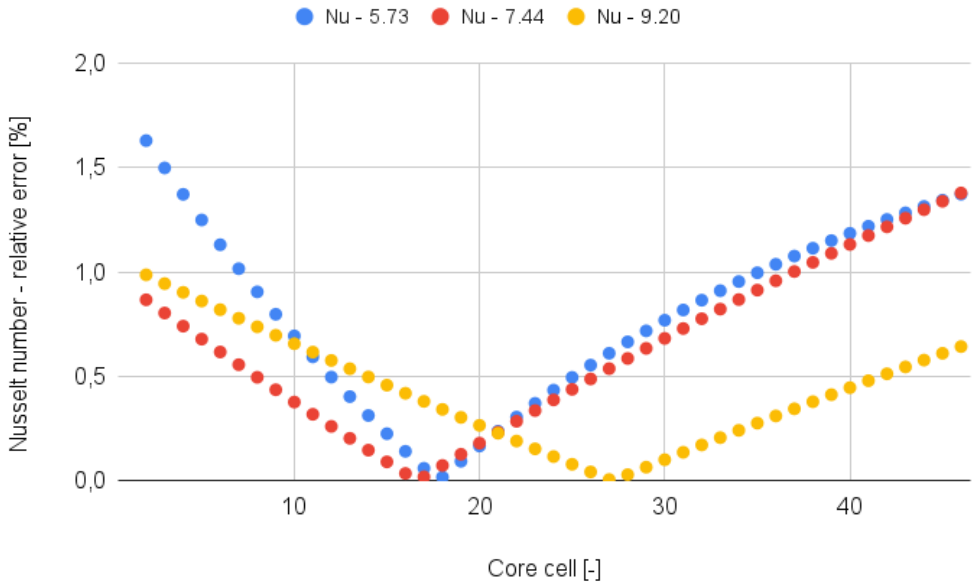

Figure 5.5: Relative errors of Nusselt number for μDEMOand mDEMO.

Using the similarity of the Nusselt numbers for the two demonstrators, the equation for forced convection was derived:

$$\begin{aligned} Fc^{\mu} &= \frac{d^{m}}{d^{\mu}} \cdot \frac{T^{\mu}}{T^{m}} \cdot \frac{k^{\mu}}{k^{m}} \cdot Fc^{m} \\ Fc^{m} &= \frac{d^{\mu}}{d^{m}} \cdot \frac{T^{m}}{T^{\mu}} \cdot \frac{k^{m}}{k^{\mu}} \cdot Fc^{\mu} \end{aligned} \tag{5.6}$$

As all parameters except the temperature difference for the minidemonstrator are known, it was decided to use a constant temperature coefficient c.

$$\begin{aligned} Fc^{\mu} &= c \cdot \frac{d^{m}}{d^{\mu}} \cdot \frac{k^{\mu}}{k^{m}} \cdot Fc^{m} \\ Fc^{m} &= \frac{1}{c} \cdot \frac{d^{\mu}}{d^{m}} \cdot \frac{k^{m}}{k^{\mu}} \cdot Fc^{\mu} \end{aligned} \tag{5.7}$$

The figure 5.6 shows the results obtained from the Cathare-2 software, calculated using the equation 5.6, and the values calculated by the equation 5.7 for a velocity of 0.5 $\frac{m}{s}$.

To make it easier to compare the results, it was decided to calculate the relative error between the calculations obtained by Cathare-2 and the results calculated using the equations. The equation is shown below:

$$\delta = \frac{|Fc^{cathare} - Fc^{calculation}|}{Fc^{cathare}} \cdot 100 \tag{5.8}$$

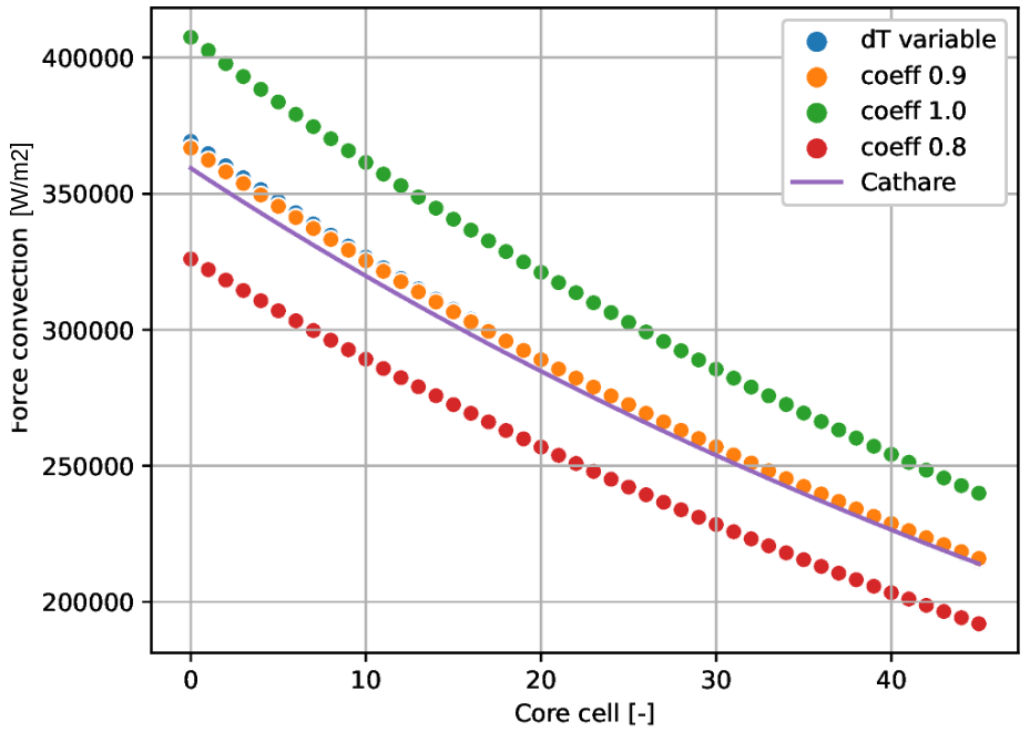

Figure 5.6: Results of forced convection for Cathare-2 calculations and calculation for equations 5.6 - 5.7

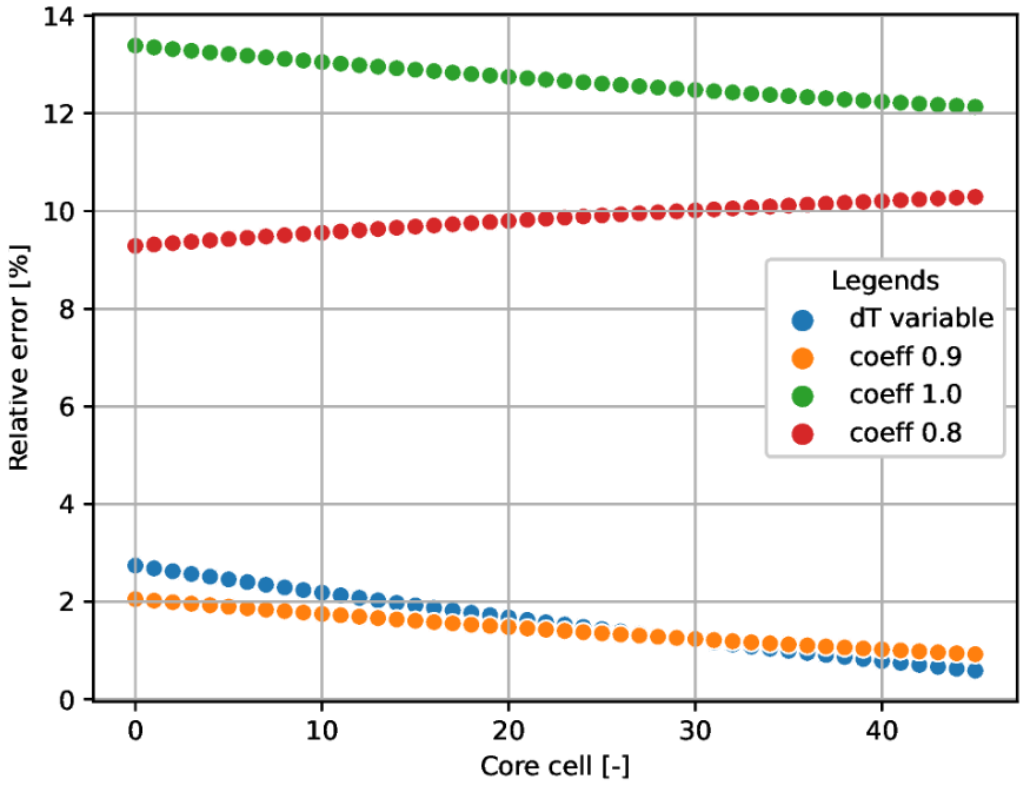

Figure 5.7: Relative errors for calculation for equations 5.6 - 5.7

Since the value of the coefficient of temperature difference can change depending on the velocity of the liquid metal flow, calculations had to be made for different cases. It was decided to perform calculations for liquid metal velocities from 0.001 to 2 $\frac{m}{s}$. The results are shown in the figure 5.8.

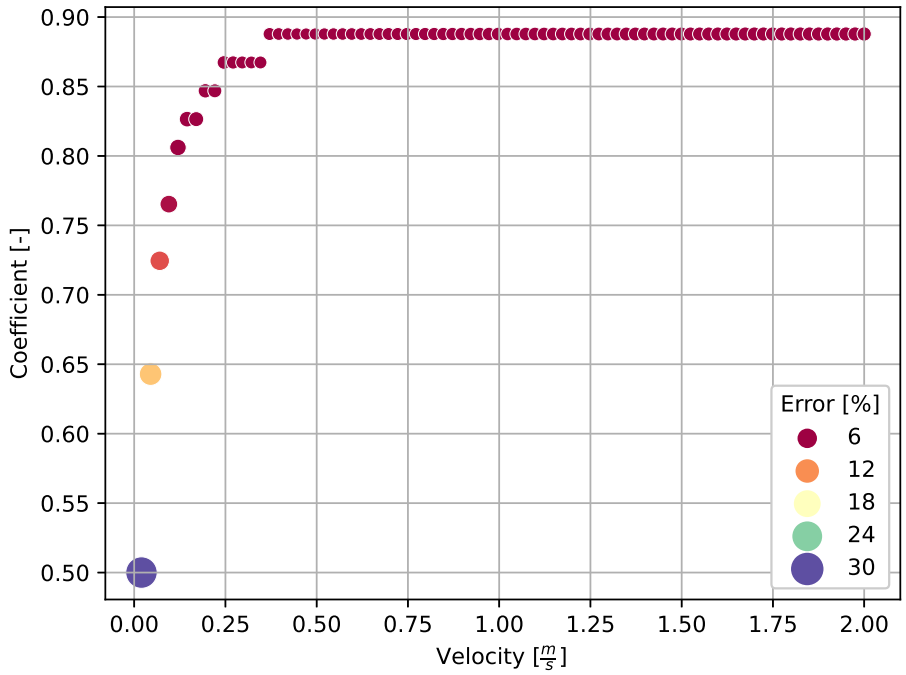

Figure 5.8: Characteristics of the relationship of the c-factor with velocity and the obtained average relative errors

5.2.2 Control of heat exchange via a pumping system

The next task that was decided was to see how flow velocity affects heat transfer. The figure 5.9 shows the model with fixed and variable parameters marked. As can be seen, the inlet temperatures for fuel and coolant are constant, while the outlet temperatures are the resultant temperatures of heat transfer. This means that the heat supplied to and received from the system is variable and selected to maintain constant input temperatures in the system. This solution is designed this way because it follows from the way the boundary condition must be implemented in Cathare-2.

The graph 5.10 shows the results for the μDEMO and mDEMO. As can be seen, as the Nusselt number increases (that is, the kinetic energy of the system increases), the

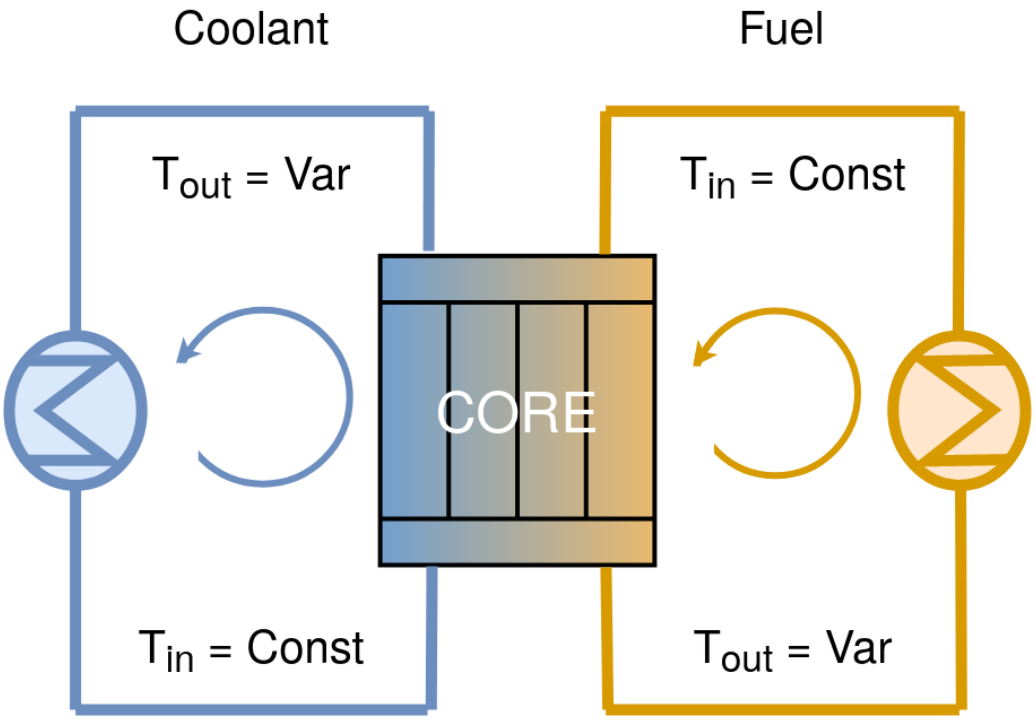

Figure 5.9: Scheme of μDEMO and mDEMO showing constant and variable temperatures.

heat transfer between the loops also increases. This means that heat transfer is strongly related to flow velocities.

Using the 5.7 equation, it was decided to check the accuracy of scalability between demonstrators. In Figure 5.11, it can be seen that the results obtained for Cathare-2 and calculations with a coefficient of 0.88 are similar to each other, but for the boundary values there are greater differences than in the middle of the relationship. In addition, the results are better for higher values of the Nusselt number than for lower values of the Nusselt number, which is consistent with the conclusions presented in chapter 5.2.1.

The figure shows the relative error to the liquid metal velocity in the cooling loop. To calculate the relative errors, the equation 5.8 was used. As can be seen, the relative error for the low value of Nusselt does not exceed 10%. On the other hand, for higher values of Nusselt, the error does not exceed 4%, which proves that the scalability depends very little on the speed of the liquid metal in the cooling loop.

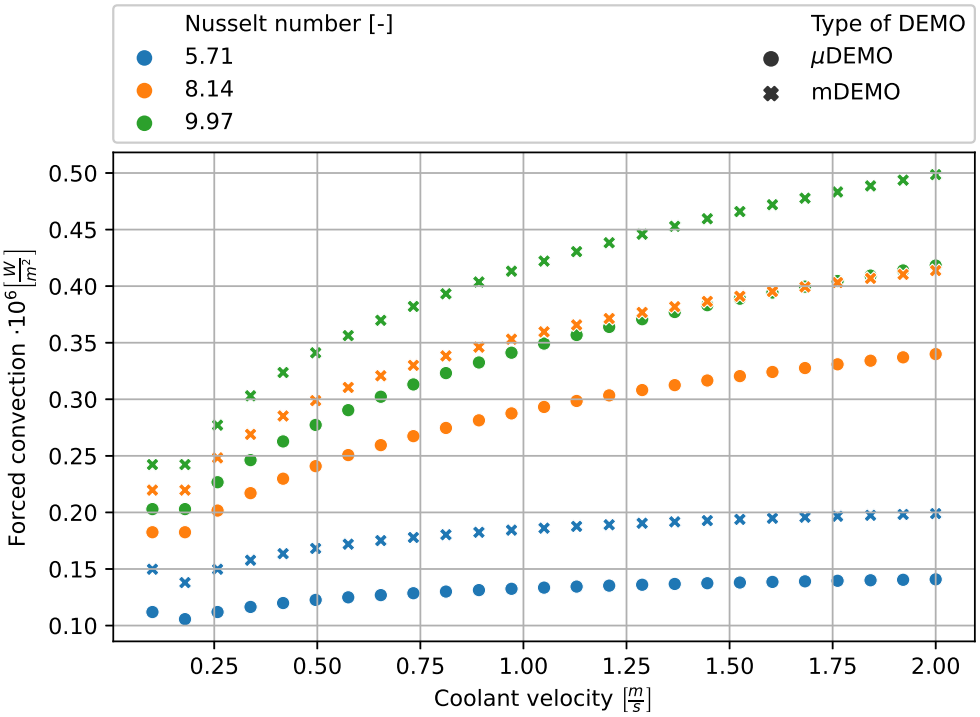

Figure 5.10: Characteristics of relationship of forced convection with coolant velocity for microdemonstrator and minidemonstrator

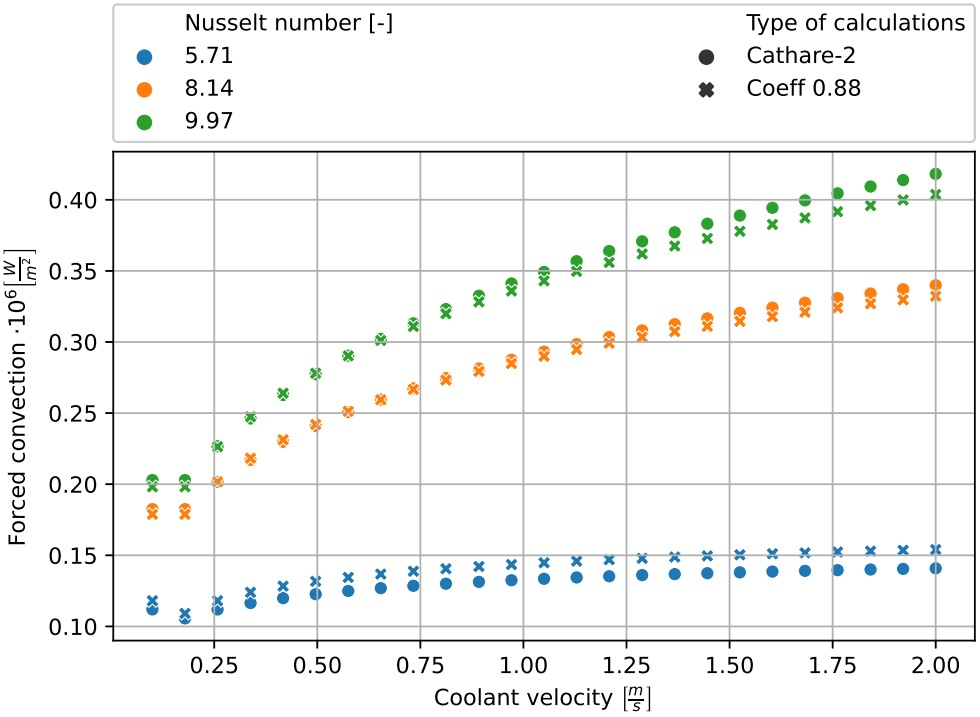

Figure 5.11: Comparison of forced convection values obtained by Cathare-2 and calculated with a c coefficient of 0.88.

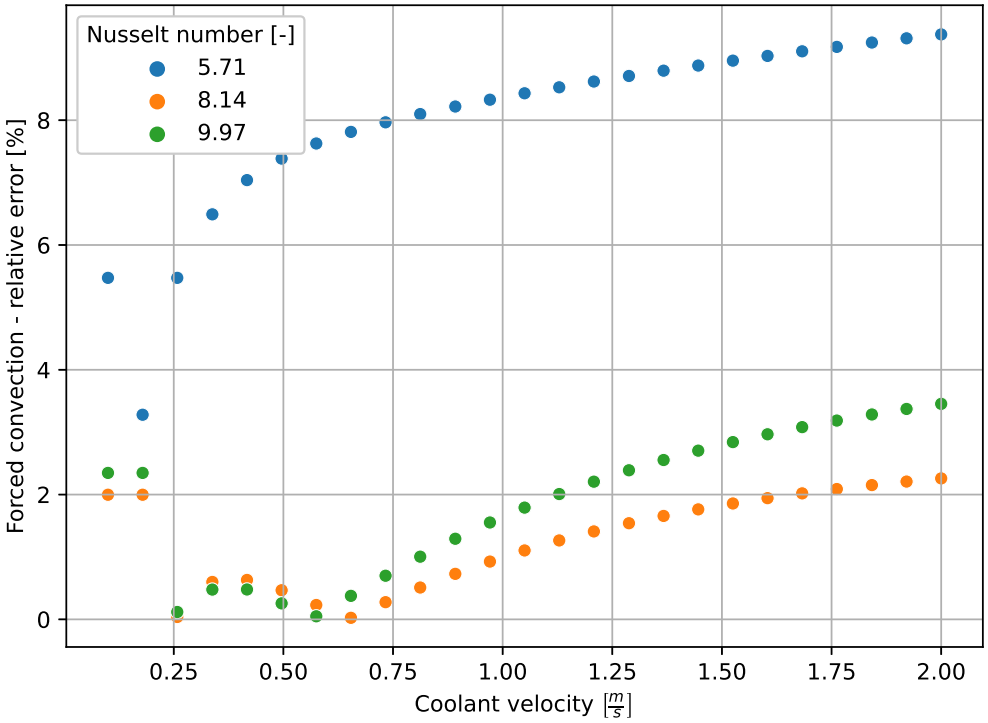

Figure 5.12: Relative error of forced convection between Cathare-2 calculations and calculations with a c factor of 0.88

Chapter 6

Magnetohydrodynamic pump optimization

This subsection focuses on optimization methods for a DC magnetohydrodynamic pump. The work presents three types of optimization - using simulated annealing alone, using SA and polynomial approximation, and using SA and multivariate regression, and finally compares the obtained results. The diagram (figure 6.1) shows the methodology used.

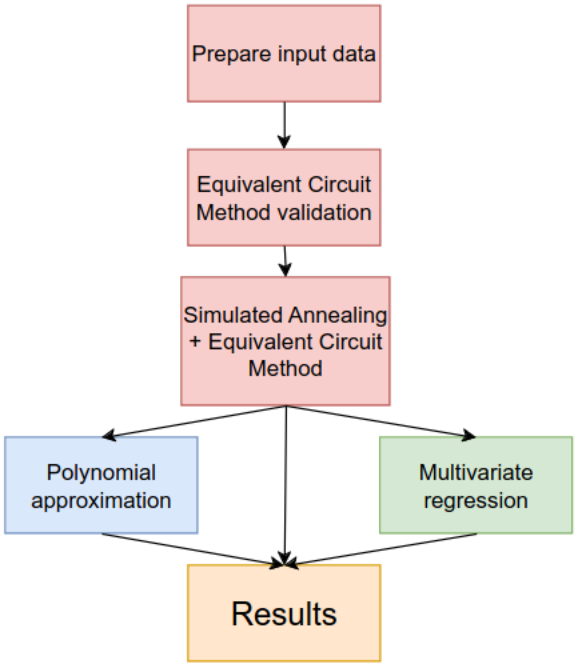

Figure 6.1: Scheme of the Magnetohydrodynamic pump optimization algorithm.

Before the ECM was used to perform the calculation and optimization of the pump for the DFR reactor, its implementation was validated.

Subsection 6.1 presents the validation of the method with examples of data used from [Lee and Kim, 2017] and [Borges et al., 2010]. Calculations for a theoretical reactor using data from the [Sierchuła et al., 2019] article were also included. The data used in validation were then used in optimization.

In subsection 6.2 optimizations were performed for all four MHD pumps, which are are presented in subsection 6.1.

In subsection 6.2.1 a multivariate regression model was created for the values obtained by the simulation algorithm annealing.

6.1 Validation of the ECM

[Lee and Kim, 2017] tested an MHD pump in an experimental loop in which the medium was liquid sodium reacting with carbon dioxide. For validation the following data from the article were used: $B_m = 0.172\ T$, $v = 0.72\ \frac{m}{s}$, $W_d = 0.0384\ m$, $H_d = 0.0018\ m$ and $L = 0.09\,m$. All of the parameters for [Lee and Kim, 2017] are shown in table 6.1. Data on some material parameters, i.e. density, resistivity, and roughness for stainless steel, which are necessary to perform the calculations, were not presented in the original paper. The density, resistivity and viscosity of sodium were taken from [Fink and Leibowitz, 1995] and [Addison et al., 1969]. For a temperature of 300 ^oC these values are: $\rho = 880.51\ \frac{kg}{m^3}$, $\mu = 3.40\ mPa \cdot s$ and $\rho' = 0.172\ \mu\Omega \cdot m$. The sodium flow rate value is $0.0005\ \frac{m^3}{s}$. However, resistivity characteristics for stainless steel pump channel walls were taken from [Ho and Chu, 1977]. These characteristics are given below.

$$\rho'_w = 9.07 \cdot 10^{-19}\ T^4 - 2.17 \cdot 10^{-15}\ T^3 + \ 1.37 \cdot 10^{-12}\ T^2 + \\ + 4.7 \cdot 10^{-10}\ T + 5.84 \cdot 10^{-7} \tag{6.1}$$

where ρ'_w and T are resistivity and temperature [K] respectively.

To obtain similar results, a resistivity value of $\rho' = 9.93\ \mu\Omega \cdot m$ and roughness of $e = 0.00015\,m$ were assumed. For the input current, the authors reported a value that equalled 116 A. After applying the above-mentioned parameters into the current implementation of the ECM, the result obtained was equal to 119.27 A.

In contrast, [Borges et al., 2010] focused on liquid lead as the working medium. The parameters of the liquid metal take the following values: $\rho = 10470\ \frac{kg}{m^3}$, $\mu = 1.78\ mPa \cdot s$ and $\rho' = 0.210\ \mu\Omega \cdot m$, while the flow rate was $0.00012\ \frac{m^3}{s}$. The following data were also

used: $B_m = 0.9\ T$, $v = 0.40\ \frac{m}{s}$, $W_d = 0.03\ m$, $H_d = 0.01\ m$ and $L = 0.07\ m$. All of the parameters for [Borges et al., 2010] are also shown in the summary table 6.1. The paper does not show how the equivalent resistances and the pump wall thickness were determined. Finally, the following values of equivalent resistance and pump wall thickness were assumed: $R_{LM} = 9.00 \cdot 10^{-6}$, $R_w = 1.01 \cdot 10^{-4}$, $R_b = 5.25 \cdot 10^{-5}$ and $d = 0.002$ m, respectively. For the input current, [Borges et al., 2010] reported a value of 800 A. As a result of calculations for the assumed values, a current ECM implementation resulted in value of 802.13 A.

On the basis of the information contained in [Sierchuła et al., 2019] a study of the applicability of a DC condensing pump in a DFR reactor, in which the fuel medium is liquid metal, more precisely, Uranium-Chromium eutectic, was performed. Since this mixture has different material properties depending on the chromium concentration, the concentration giving the lowest melting point was chosen. This means the following mass proportion of the components: Cr – 4.78 %, ^{235}U – 12.80 %, ^{238}U – 82.42 % weight [Okamoto, 2012]. For such eutectic in the article [Sierchuła et al., 2019] neutron calculations were realized. Finally, MHD pump calculations for the fuel loop for the DFR reactor were carried out with data taken from the article [Sierchuła et al., 2019]. Assuming a power of 250 MW, a wall material of loop- TZM alloy (99.4% molybdenum, 0.5% titanium, 0.08% zirconium, 0.02% carbon), a liquid metal velocity of 0.5 $\frac{m}{s}$, an eutectic density of 15634 $\frac{kg}{m^3}$, with a temperature equal to 1100^oC and for a loop cross section of 0.1212 m^2 a flow rate of 0.06 $\frac{m^3}{s}$ was obtained. Due to the large cross section value, it was decided to use a parallel 12 pumps system with smaller cross sections ($A = 0.01\ m^2$). For the resulting flow rate, a pump operating temperature of 1100 ^oC and assuming a generated pressure by the pump equal to 15000.0Pa, the following geometry was assumed: $W_d = 0.2$ m, $H_d = 0.05$ m, L = 0.5 m, $d = 0.001$ m and $B_m = 1$ T. The input current value for the listed parameters aquired by out ECM implementation was found to be 9.8 kA.

Since no more parameters of the Uranium-Chromium eutectic were given in [Okamoto, 2012] or any literature item, information from [Finucane and Olander, 1969] for chromium concentrations in the mixture of 2.2 and 4.1% was used to obtain the density and dynamic viscosity, followed by linear extrapolation.

The exact resistivity of this eutectic was also not investigated, so the data for charac-

terization was taken from [Provow and Fisher, 1964] for a concentration of 4.97 %. The resulting approximated material parameter characteristics for the fuel are presented below.

$$\begin{aligned} \rho &= 1000(-0.00088\ t + 16.69), \\ \rho' &= (0.02\ t + 57.61) \cdot 10^{-6}, \\ \mu &= -6.42 \cdot 10^{-8}\ t^3 + 0.00027\ t^2 - 0.389\ t + 195.46, \end{aligned} \tag{6.2}$$

where, ρ, ρ', μ and t, are density, resistivity, dynamic viscosity and temperature $[^oC]$, respectively.

Using the above characteristics, it was assumed that for 1100 ^oC the material values for the Uranium-Chromium eutectic are: $\rho = 15722\ \frac{kg}{m^3}$, $\mu = 8.81\ mPa \cdot s$ and $\rho' = 79.62\ \mu\Omega \cdot m$.

However, resistivity characteristics for molybdenum alloy pump channel walls were taken from [Desai et al., 1984]. These characteristics are given below.

$$\rho'_w = (4.42 + 0.0258 * t + 1.56 \cdot 10^{-6} \cdot t^2) \cdot 10^{-8} \tag{6.3}$$

where ρ'_w and t are resistivity and temperature respectively. For 1100^oC the resistivity of the molybdenum material is 1.2 $\mu\Omega \cdot m$.

The last pump to be analyzed is the DFR reactor coolant loop pump. The liquid metal that will be pumped is lead. The lead parameters for a temperature of 800 ^oC are $\rho = 10449\ \frac{kg}{m^3}$, $\mu = 1.23\ mPa \cdot s$ and $\rho' = 0.118\ \mu\Omega \cdot m$. The parameters for the pump are as follows: $B_m = 1\ T$, $v = 2\ \frac{m}{s}$, $A = 0.01\ m^2$, $W_d = 0.2\ m$, $H_d = 0.05\ m$ and $L = 0.5\ m$. The input current value for the listed parameters aquired by out ECM implementation was found to be 10.1 kA.

All parameters for fuel pump and coolant loop are also shown in the summary table 6.1.

6.2 Optimization

This subsection focuses on describing the results of the geometries optimization of the four MHD pumps that were used so far.

Table 6.1: Comparison of the values from the articles to the results obtained

	[Lee and Kim, 2017]	[Borges et al., 2010]	Fuel loop	Coolant loop
Medium	Na	Pb	U-Cr	Pb
t	300.0	500.0	1100.0	800.0
ρ	880.51	10470	15722	10449
v	3.40	1.78	8.81	1.23
ρ' $[\cdot 10^{-7}]$	1.72	2.1	796.2	11.80
ρ'_w $[\cdot 10^{-7}]$	9.93	10.88	12.00	3.47
$\dot{m}$	0.044	1.260	78.61	208.98
ΔP	5000.0	34600.0	15000.0	15000.0
R_{ver} $[\cdot 10^{-4}]$	1.30	0.35	0.26	0.26
d	0.001	0.0025	0.001	0.001
S $[\cdot 10^{-3}]$	0.0069	0.3	10	10
W_d	0.0384	0.03	0.2	0.2
H_d	0.0018	0.01	0.05	0.05
L_d	0.09	0.07	0.5	0.5

In MHD pumps, the width, height, and length of the pump channel were variables to be optimized. On the other hand, the parameter to be minimized was the input current. In the calculations, it was assumed that parameters such as the cross-section of the pump channel, magnetic induction, flow rate, velocity, liquid metal flow rate, and pressure drop across the other loop elements were held constant.

Magnetic induction is not included in the optimization even though there is a local minimum for magnetic induction as well (Figure 6.2). This is because from an economic point of view, the stronger the magnet the higher the price, so it is cheaper to build a pump with an optimized geometry than to use expensive, stronger magnets.

Different parameters of the simulated annealing algorithm were tested to achieve the best results for minimizing the input current to the MHD pump.

The best results for [Lee and Kim, 2017] were obtained for iteration equal to 1000 and step equal to 0.114, for [Borges et al., 2010] the respective values were 500000 and 0.176, and for fuel and coolant pump 500000 and 0.166 respectively.

However, in order to speed up the computation, it was decided to use 5000 iterations

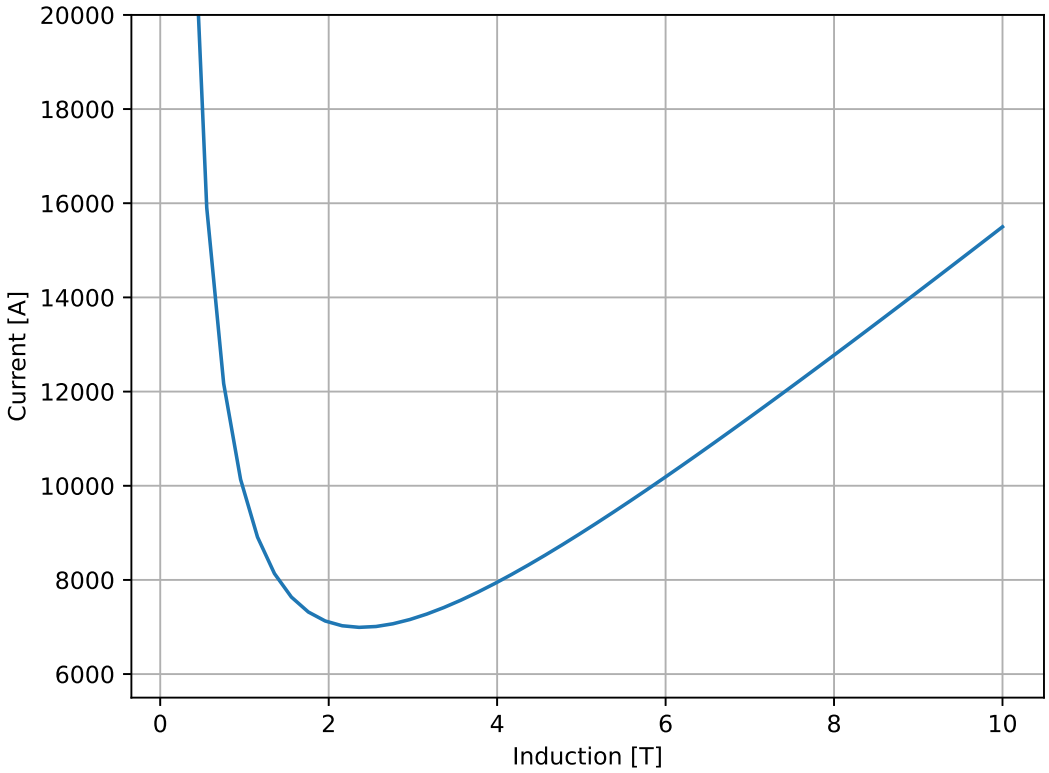

Figure 6.2: Dependence of input current on magnetic induction

with step equal to 0.166, and execute the algorithm 100 times and choose the best result obtained. This solution is protected against obtaining a false minimum result. The probability of acceptance in simulated annealing algorithm varied from 0.9 to 0.015.

The table 6.2 shows the final results of the optimized DC MHD pumps and obtained minimum values of the input currents. It is worth noting, that the algorithm reduced the length of the pump, while the pressure generated by the pump is constant.

Table 6.2: Optimal current values

	[Lee and Kim, 2017]	[Borges et al., 2010]	Fuel pump	Coolant pump
W_d	0.0691	0.2326	0.4483	0.4711
H_d	0.0010	0.0013	0.0223	0.0212
L	0.0495	0.0455	0.1037	0.1122
I	92.55	490.47	8400.39	8410.15
ρ''	$1.9{\cdot}10^6$	$8.29{\cdot}10^6$	$3.63{\cdot}10^6$	$3.54{\cdot}10^6$
Φ	50.29	85.04	21.51	18.92

Figure 6.3 shows the dependence of the individual pressure components for the pump calculation for fuel pump. It is noteworthy that despite the increase in pressure generated ΔP_w and electrical losses ΔP_e and hydrodynamic losses ΔP_h, the total pressure ΔP is constant at 15000 Pa. This means that by reducing the length of the pump, we reduce the losses that must be compensated by the additional work. Bottom Figure 6.3 shows a

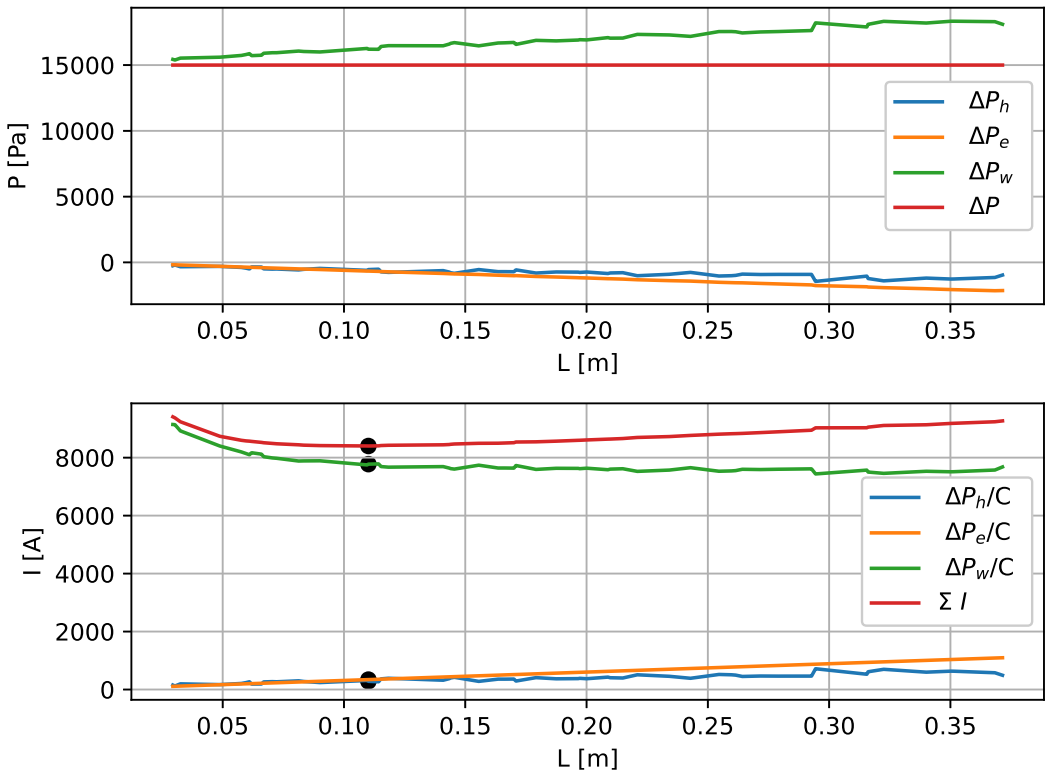

Figure 6.3: Dependence of optimized pressures (generated and losses) on pump channel length, and dependence of optimized currents and sum of currents (input current) on pump channel length.

similar relationship as the top figure 6.3, however, the coefficients have been converted to the current to be supplied to the MHD pump and the sum of all the individual currents is shown as well. The bottom plot of Figure 6.3 shows the very dependence of the optimized input current on the pump length. The points highlighted in black represent the minimum input current, which is 8400.39A for a pump channel length of 0.1037m. It is worth noting that as the length increases, the current needed to generate the generated pressure ($\frac{\Delta P_w}{C}$) decreases, while the currents needed to negate the electrical ($\frac{\Delta P_e}{C}$) and hydrodynamic ($\frac{\Delta P_h}{C}$) losses of the MHD pump increase. As a result (Fig. 6.4), the minimal currents has the shape of a complex polynomial; however, in the close vicinity of the minimum (length

range between 0.08 and 0.14 m — which is shown in blue in the graph), the minimal currents can be approximated by a polynomial of the second degree. This means that one cannot aim to keep the pump length as short as possible, because there is a limit below which further decreasing the pump length increases the current that would need to be delivered to the MHD pump.

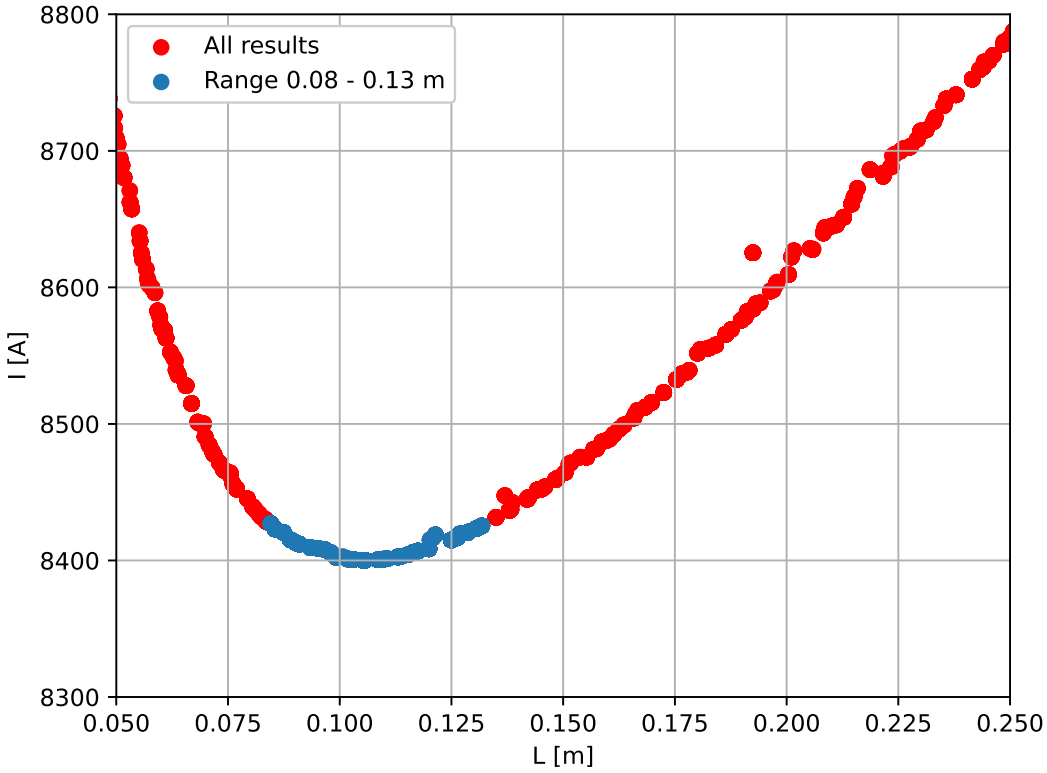

Figure 6.4: Results of minimum current obtained by simulated annealing on pump channel length.

After selecting points in the range of 0.08 and 0.13 m, a second-order polynomial approximation was used to obtain even more accurate current minimization. To achieve this, two relationships had to be determined: the current function on the pump channel length and the current characteristic on the current flux delivered to the electrodes. The general equations of the polynomials were presented in equations 6.4, while the coefficient values for [Lee and Kim, 2017], [Borges et al., 2010] and [Sierchuła et al., 2019] were placed in table 6.3.

$$I = a_L L^2 - b_L L + c_L$$
$$I = a_{\rho''} \rho''^2 - b_{\rho''} \rho'' + c_{\rho''} \tag{6.4}$$

Table 6.3: Coefficients for second degree polynomials

	a_L	b_L	c_L	$a_{\rho''}$	$b_{\rho''}$	$c_{\rho''}$
[Lee and Kim, 2017]	4170	-416	103	0.33e-11	-0.12e-4	104
[Borges et al., 2010]	50900	-4570	593	0.22e-12	-0.39e-5	508
Fuel pump	35300	-7490	8800	0.1e-10	-0.82e-4	8570
Coolant pump	32800	-7430	8930	0.11e-10	-0.08e-3	8550

By calculating the roots of the derivatives, the minimum values of the function were determined Eq. 6.4. Then, having the optimum length from the first characteristic, and the minimum current and optimum current flux, the height value can be determined from the Eq. 6.5.

$$\rho' = \frac{I}{H_d L} \tag{6.5}$$

Then using the equation for the area, the value of the pump channel width was determined, thus obtaining the optimal geometry. The difference between the currents obtained from the simulation annealing and the approximated polynomials is less than 0.1%. Comparing the results of each step, i.e., from the simulated annealing, the minimum of the approximated polynomials, and from the calculated geometry, they differ slightly (less than 0.1% relative error); however, it was possible to obtain a reproducible result from the random method used. For polynomial approximation, the obtained minimum current values for [Lee and Kim, 2017], [Borges et al., 2010], fuel pump and coolant pump were: 93.26A, 490.72A, 8404.68A and 8412.15A, respectively. The order of all the equations used to calculate the pump channel geometry and the parameter that was determined from them are shown below:

1. $L = \frac{-b_L}{2a_L}$
2. $\rho'' = \frac{-b_{\rho''}}{2a_{\rho''}}$
3. $I = a_{\rho''}\rho''^2 + b_{\rho''}\rho'' + c_{\rho''}$
4. $H_d = \frac{I}{\rho'' L}$
5. $W_d = \frac{S}{H_d}$

To further simplify the optimization problem, multivariate regression was also used. This model converts the multivariate problem into an equation with multiple independent variables.

6.2.1 Multivariate regression

Current minimization results obtained by simulated annealing were used to determine the multivariate regression. The universal model for the four pumps is shown below (Eq. 6.6). The regression model was used to determine the width and length of the pump channel, while the height is calculated from the cross section of the pump channel.

$$\begin{aligned} W_d &= a_1 + b_t t + b_{\Delta P}\Delta P + b_A A + b_v v - b_B\sqrt{B} \\ H_d &= \frac{S}{W_d} \\ L &= a_2 + b_{t2} t + b_{\Delta P2}\Delta P + b_{A2} A + b_{v2} v - b_{B2}\sqrt{B} \end{aligned} \tag{6.6}$$

Tables 6.4 and 6.5 present the individual coefficients for four regression models for width and height respectively.

Table 6.4: Multivariate pump channel width regression coefficients and fit coefficients

	a_1	$b_t[10^{-7}]$	$b_{\Delta P}[10^{-7}]$	b_A	b_v	b_B
[Lee and Kim, 2017]	0	0	0	1000	0	0
[Borges et al., 2010]	−0.006	117	2.24	963.45	−0.052	0.021
Fuel pump	−0.04	673	85.5	31.75	−0.514	0.180
Coolant pump	0.327	59.0	94.3	30.22	−0.166	0.0064

Table 6.5: Multivariate pump channel length regression coefficients and fit coefficients

	a_2	$b_{t2}[10^{-7}]$	$b_{\Delta P2}[10^{-7}]$	b_{A2}	b_{v2}	b_{B2}
[Lee and Kim, 2017]	0.105	84.3	43.4	315.99	−0.037	−0.176
[Borges et al., 2010]	0.088	38.5	5.39	64.02	−0.062	−0.061
Fuel pump	0.229	485	35.5	4.23	−0.134	−0.178
Coolant pump	0.317	16.3	42.1	4.39	−0.041	−0.203

A multivariate coordinate grid was generated to determine the equation coefficients of the multivariate regression model, with ranges were ±20% for reference temperature and $-20\% + 50\%$ for the other values used in the original publications (Table 6.6). The reference temperatures are those for which previous calculations were performed and are listed in table 6.1.

Such created data set contained 1024 items for each analysed pump. Simulated annealing was performed for each point to obtain the optimized geometry. Then multivariate regression was applied to the numerous optimised geometries of considered pumps. Lastly, multivariate regression model was used on the initial grid values in order to acquire optimised geometries. Such generated geometries were run through ECM implementation and values of the currents were compared with values of currents acquired by simulated annealing.

Table 6.6: The range of applicability of multivariate regression models

	[Lee and Kim, 2017]	[Borges et al., 2010]	Fuel loop	Coolant loop
#	1024	1024	1024	1024
medium	Na	Pb	UCr	Pb
t	240 - 360	400 - 600	880 - 1320	640 - 960
ΔP	4000 - 7500	27680 - 51900	12000 - 22500	12000 - 22500
A	$(5.5 - 10.4) \cdot 10^{-6}$	$(0.24 - 0.45) \cdot 10^{-3}$	0.008 - 0.015	0.008 - 0.015
v	0.58 - 1.08	0.32 - 0.6	0.4 - 0.75	1.6 - 3
B	0.14 - 0.26	0.72 - 1.35	0.8 - 1.5	0.8 - 1.5

The violin plot shows the relative error of current density distribution of the MHD pump current minimization for the regression models (figure 6.5). The vertical lines represent the minimum, median and maximum value of the obtained results, respectively. The rectangle inside the violin plots denote the range between percentile 5 % and 95 %. Negative values of relative errors of current minimization indicate that the regression model achieved a lower current value than the simulated annealing.

The maximum error does not exceed 10 % and the 95th percentile does not exceed 1 % for four pump models. The exact percentiles are shown in table 6.7.

Regression models achieve very small errors only when the parameters of the pump being sought are within the applicability range of the model. Using a regression model

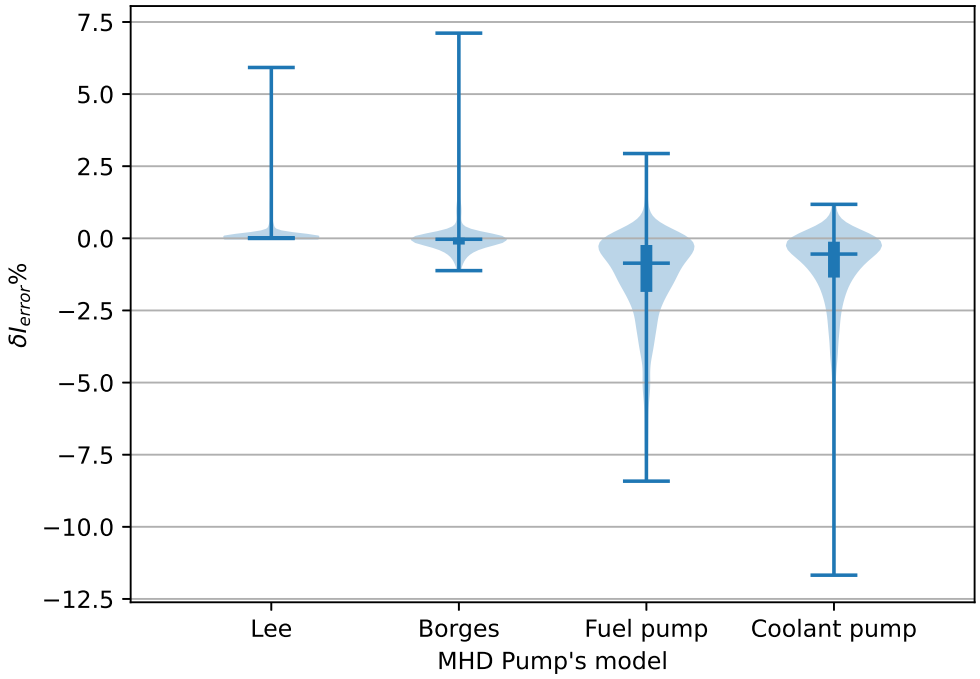

Figure 6.5: Violin plot for relative errors for individual pumps

Table 6.7: Percentiles for relative minimum current errors

	0%	5%	50%	95%	100%
[Lee and Kim, 2017]	$-3.21 \cdot 10^{-3}$	$-2.53 \cdot 10^{-4}$	0.02	0.39	5.92
[Borges et al., 2010]	-1.12	-0.62	-0.03	0.77	7.11
Fuel loop	-8.42	-3.98	-0.86	0.15	2.94
Coolant loop	-11.68	-3.59	-0.55	0.17	1.18

outside the range can cause the results to have large errors relative to the results from simulated annealing.

The table 6.8 shows the current value obtained during validation (I_{val}), and the minimum current values obtained by all of the listed methods: I_{SA} - minimum current obtained by simulated annealing, I_{PA} - minimum current obtained by polynomial approximation, I_{MR_2} - minimum current obtained by multivariate regression.

Table 6.8: Summary of all minimum currents calculated by different methods

	I_{val}	I_{SA}	I_{PA}	I_{MR}
[Lee and Kim, 2017]	119.27	92.55	93.26	92.48
[Borges et al., 2010]	802.13	490.47	490.72	492.70
Fuel pump	9800	8400.39	8404.68	8427.63
Coolant pump	10052	8410	8412.68	8434.87

6.3 Flow velocity dependence

Analyzing the results for the fuel and cooling loops of the DFR reactor, it can be seen that the current values are higher than for the other pumps analyzed. This is most visible for the fuel loop pump. One reason for this is that the cross sections of the Lee and Borges pumps are relatively smaller than for both DFR loops. The graph 6.6 shows the dependence of the input currents to the liquid metal velocity. The higher the velocity, the higher the current to be supplied to the MHD pump. This means that you can control the velocity of the liquid metal in the loop by varying the current supplied to the pump.

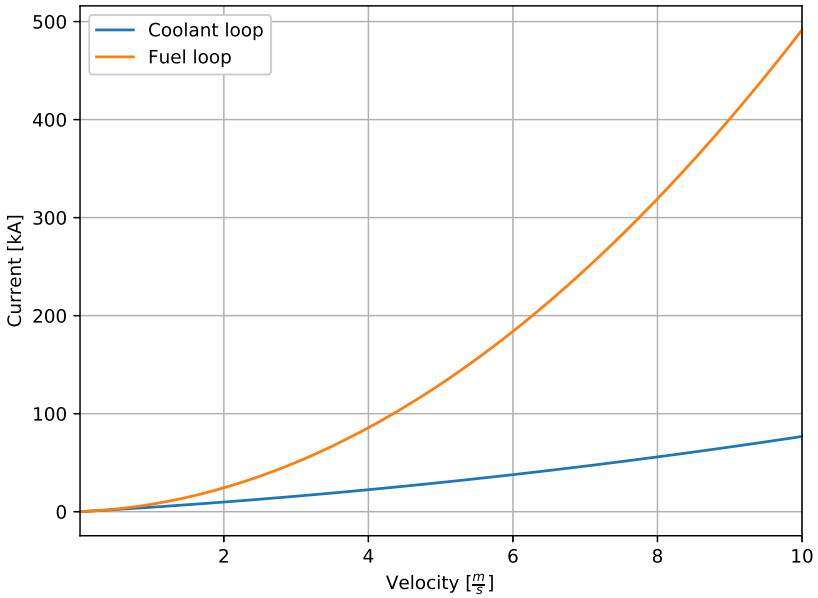

Figure 6.6: Relationship of velocity and current for fuel and coolant loops.

The resistivity of the pumped medium and the resistivity and thickness of the pump channel have a great influence on the current value. When designing MHD pumps, it should be targeted that the resistivity of the pump wall material is close to or greater

than the resistivity of the liquid metal. Otherwise, more of the current will flow through the channel walls than the liquid metal. The resistivity of the Uranium-Chromium eutectic is $\rho' = 79.62\ \mu\Omega \cdot m$ and resistivity of molybdenum is $1.2\ \mu\Omega \cdot m$. Therefore, to reduce the current value for the fuel pump, it would be necessary to use a suitable material with higher resistivity (e.g. tungsten alloy), or even to make the pump channel out of ceramic.

Table 6.9 compares material resistivities and the input current results for various materials that are applicable at high temperatures ([Voorde and Division, 1983]) for 1100 ^oC. The higher the resistivity of the pump wall material, the lower the current required to drive the magnetohydrodynamic pump.

Table 6.9: Current results for different MHD pump wall materials

Material	Resistivity $[10^{-8}\Omega m]$	I_{SA} [A]
Molybdenium (TZM)	34.7	8400.39
Tungsten	36.6	8021.99
Tantalum	57.6	5412.90
Hafnium	158	2432.49

Chapter 7

Conclusions and discussions

The present Ph.D. thesis is related to the new DFR nuclear reactor concept. This work will be included in the DFR-related safety report created by DFE. Its purpose was to develop tools for analyzing the pumping system and to prove that the pumping system is an indispensable component of DFR safety. Accordingly, it was proven that changing the flow rate affects reactivity and heat transfer in the reactor core. The thesis also decided to perform calculations for demonstrators, since the computational tools prepared for these devices will be necessary for the analysis and design of the final DFR concept. In addition, an as yet undiscussed problem is the design of the MHD pump for such high temperatures as will be encountered in the DFR. Another thing that has been proven is that the design of the pump channel has a significant impact on the current needed to force the flow of liquid metal, and thus on the electrical power to be supplied to the MHD pump. Therefore, it was decided to do a minimization calculation for the input current. The solutions presented in the thesis are not only new ways to solve the assumed problems, but they will also be applicable to other liquid metal-based nuclear reactors.

The section 5 presents the scalability problem for the demonstrators. The goal of the task was to develop a way to estimate the parameters of one demonstrator using the results obtained from the other device. With such tools, it would also be possible to estimate values and parameter changes even for the demonstrator and DFR. The task was complicated because there are as many as three fundamental differences in the two demonstrators - a difference in size, a difference in temperature, and the different liquid metals considered. Typically, dimensionless numbers are used in cases where only one of

the previously mentioned differences is present.

Analyzing the results for similarity of Reynolds numbers, it can be seen that for μDEMO, we have to use a larger diameter by 1.5, and higher velocities by 3.4, to get the same Reynolds number. This means that the flow rate must be increased by as much as 2.25 times. On the other hand, analyzing the results for similarity of Reynolds numbers, you can see that for μDEMO we need to use a smaller diameter by 0.6, and the velocities should stay the same as for μDEMO to get the same Nusselt number. This means that the flow rate must be decreased by as much as 0.36 times.

Then, it was decided to use the similarity of Nusselt numbers and, based on the results obtained for the μDEMO , estimate the value of forced convection for the mDEMO. During the analysis, it was noted that the only unknown was the ratio of temperature differences between the μDEMO and mDEMO, so it was decided to introduce an additional coefficient c and perform a mathematical analysis to estimate its value. After the calculations, it was found that for higher speeds, the c-factor has a value of 0.88, and the average difference in results between the calculations and the results from Cathare does not exceed 6% while for speeds from 0.01 to 0.4 m/s, the value of the coefficient varies from 0.5 to 0.88 and the higher the speed, the smaller the relative error.

The results obtained from the calculations would have to be compared with the experimental results. This will be done in the future when the μDEMO and mDEMO are built. Then it will be possible to check the correctness of the calculations and make corrections to the models. In the future, calculations should also be made for two-phase flow, since the Demonstrators and also the DFR will have argon in addition to liquid metal. This gas will be used to fill the fuel and cooling loop, so it should also be included in the calculations. In addition, future calculations could be made to account for the formation of microcrystals of eutectic in liquid metal. They can be formed due to local temperature fluctuations. Such structures can also affect the flow parameters and also the performance of the magnetohydrodynamic pump.

Calculations were also performed to see how the flow velocity affects heat transfer between loops. At first, a test was done, changing only the flow velocity in the fuel loop and it was noticed and an increase in heat transfer. This increase is because the inlet temperature to the core is constant under the assumptions and initial conditions.

In the future, it would be necessary to do calculations in which not the inlet tempera-

ture, but the power supplied to the liquid metal. This would make it possible to analyze how heat would be transferred from the heating element to the core.

The section 6 presents a number of interesting results for the four pumps used by [Lee and Kim, 2017], [Borges et al., 2010] and [Sierchuła et al., 2019].

The first is the validation of the Equivalent Circuit Method implementation, which enabled estimation of geometry for the DC MHD pump for the DFR reactor. Then, through simulated annealing, the geometries for the four pumps were optimized so that the supplied current was as low as possible. With the results obtained, it was possible to propose a simplified design scheme for magnetohydrodynamic pumps. Finally, in order to obtain a more general models for obtaining geometries in which the supplied current is as small as possible, an input parameter space was created and optimized in simulated annealing. The resulting optimized geometries, were correlated using a multivariate regression method. It is also shown that the current values for the geometries obtained from the regression models were very close to the currents obtained from simulated annealing. The presented regression models for the four pumps yield well optimized geometries for three different operating working fluids under different operating conditions without the need to realize simulated annealing calculations.

The calculations presented in this thesis prove that the geometry of the pump channel is very important for the supplied current. Therefore, when designing a DC magnetohydrodynamic pump, it is necessary to determine the optimum pump geometry, so that the cost of the pump can be reduced (since one would have to build a power supply for high currents and low voltages) and its use. It could be also shown that the absolute value of the electric current is larger for the fuel loop than for the coolant one, which results from a much higher resistivity of the uranium-chromium eutectic compared to the liquid lead. Generally, a strong increase of the liquid metal resistivity with temperature (see Table 4.1) leads to very large current values that could be disadvantageous for application of MHD pumps for the dual fluid reactor, even if the real flow velocities are much lower than 2 m/s assumed for the regression calculations. In the case of the fuel, the flow velocity could be even reduced down the natural convection. Nevertheless, the method we propose to reduce the applied current is simply to increase the resistivity of the pump channel by using a high-resistance liner (e.g. a ceramic element) along the pumping length, which

would automatically increase the current through the liquid metal.

Analysing the results obtained, it can be observed that for [Lee and Kim, 2017] and [Borges et al., 2010] the pump channel height reaches a value of 1 mm while the widths are 69.1 mm and 299 mm, respectively. This is probably due to the highly simplified flow model that is responsible for the pressure drop calculations. The flow model used does not take into account small-scale phenomena such as the thickness of the boundary layer, which can affect the pressure drop values. Therefore, further work will focus on updating the implementation of the ECM to account for such phenomena. This research will focus on CFD analyses of different operating media for very small cross sections with different flow rates.

This work presented a mathematical model for idealized MHD pump, so phenomena such as non-uniform distribution of magnetic and electric fields and Curie temperatures for the magnets have not been considered. However, these phenomena will need to be taken into account if actual MHD pump is going be constructed for the DFR fuel loop. Such problems may be solved with use of electromagnets and an open core of ferromagnetic material. On the other hand, the analysis of magnetic and electric field distribution will be performed by numerical methods i.e. CFD, in the future.

The dissertation presents innovative ways to solve the problems mentioned in the Ph.D. thesis, however, it does not exhaust the entire subject.

In the future, the presented Cathare-2 models and also the ECM should be improved, based on future experiments. In addition, it would be worth considering whether it would be possible to implement the ECM directly into the Cathare-2 code so that it would be possible to analyze the pumping system more accurately. The calculations presented in the paper could be supplemented using CFD, as well as the Finite Elements Method to analyze the electromagnetic field in the MHD pump. Once the CFD and FEM calculations are combined, an accurate flow velocity profile could be determined, and it would be possible to analyze how the pump design affects the velocity profile.

Bibliography

[Addison et al., 1969] Addison, C. C., Creffield, G. K., Hubberstey, P., and Pulham, R. J. (1969). Electrical resistivity of liquid and solid sodium. *J. Chem. Soc. A*, pages 1482–1487.

[Al-Habahbeh et al., 2016] Al-Habahbeh, O., Al-Saqqa, M., Safi, M., and Abo Khater, T. (2016). Review of magnetohydrodynamic pump applications. *Alexandria Engineering Journal*, 55(2):1347 – 1358.

[Alemberti et al., 2014] Alemberti, A., Smirnov, V., Smith, C. F., and Takahashi, M. (2014). Overview of lead-cooled fast reactor activities. *Progress in Nuclear Energy*, 77:300 – 307.

[Alpy et al., 2016] Alpy, N., Marsault, P., Anderhuber, M., Gerschenfeld, A., Sciora, P., Kadri, D., Perez, J., and Lavastre, R. (2016). Phenomenological investigation of sodium boiling in a sfr core during a postulated ulof transient with cathare 2 system code: a stabilized boiling case. *Journal of Nuclear Science and Technology*, 53(5):692–697.

[Anderhuber et al., 2015] Anderhuber, M., Gerschenfeld, A., Alpy, N., Mañes, J., and Seiler, J. (2015). Simulation of gr19 sodium boiling experiments with cathare 2 system code and trio-u mc subchannel code. *NURETH-16, 16th International Topical Meeting on Nuclear Reactor Thermal Hydraulics at Chicago*.

[Becker et al., 2007] Becker, B., Fratoni, M., and Greenspan, E. (2007). Transmutation performance of molten salt versus solid fuel reactors (draft). *The Proceedings of the International Conference on Nuclear Engineering (ICONE)*, 2007.15.

[Borges et al., 2007] Borges, E., Braz Filho, F., and Guimarães, L. (2007). Space reactor lithium flow control viability by dc electromagnectic pump. *International Nuclear Atlantic Conference - INAC*.

[Borges et al., 2003] Borges, E. M., Filho, F. A. B., and Guimarães, L. N. F. (2003). Software for dc electromagnetic pump simulation - bemc-1. *17th International Congress of Mechanical Engineering*.

[Borges et al., 2010] Borges, E. M., Filho, F. A. B., and Guimarães, L. N. F. (2010). Liquid metal flow control by dc electromagnetic pumps. *Revista de Engenharia Térmica*, 9(1-2).

[Bubelis et al., 2017] Bubelis, E., Tosello, A., Pfrang, W., Schikorr, M., Mikityuk, K., Panadero, A.-L., Martorell, S., Ordóñez, J., Seubert, A., Lerchl, G., Stempniewicz, M., Alcaro, F., De Geus, E., Delmaere, T., Poumerouly, S., and Wallenius, J. (2017). System codes benchmarking on a low sodium void effect sfr heterogeneous core under ulof conditions. *Nuclear Engineering and Design*, 320:325–345.

[Černý, 1985] Černý, V. (1985). Thermodynamical approach to the traveling salesman problem: An efficient simulation algorithm. *Journal of Optimization Theory and Applications*, 45(1):41–51.

[Desai et al., 1984] Desai, P. D., Chu, T. K., James, H. M., , and Ho, C. Y. (1984). Electrical resistivity of selected elements. *Journal of Physical and Chemical Reference Data*, 13.

[Dunn and Wei, 1988] Dunn, F. E. and Wei, T. Y. (1988). The role of sassys-1 in lmr (liquid metal reactor) safety analysis.

[Fink and Leibowitz, 1995] Fink, J. K. and Leibowitz, L. (1995). Thermodynamic and transport properties of sodium liquid and vapor. *Technical report*. Argonne National Lab. (ANL), Argonne, IL (United States).

[Finucane and Olander, 1969] Finucane, J. and Olander, D. (1969). The viscosity op uranium and two uranium-chromium alloys. *Lawrence Berkeley National Laboratory*.

[Friedlander, 2006] Friedlander, S. (2006). Stability of flows. In Françoise, J.-P., Naber, G. L., and Tsun, T. S., editors, *Encyclopedia of Mathematical Physics*, pages 1–7. Academic Press, Oxford.

[Geffraye et al., 2011] Geffraye, G., Antoni, O., Farvacque, M., Kadri, D., Lavialle, G., Rameau, B., and Ruby, A. (2011). Cathare 2 v2.5_2: A single version for various

applications. *Nuclear Engineering and Design*, 241(11):4456–4463. 13th International Topical Meeting on Nuclear Reactor Thermal Hydraulics (NURETH-13).

[Hampshire, 2018] Hampshire, D. P. (2018). A derivation of maxwell's equations using the heaviside notation. *Philosophical Transactions of the Royal Society A: Mathematical, Physical and Engineering Sciences*, 376(2134):20170447.

[Hanusek and Macian-Juan, 2022] Hanusek, T. and Macian-Juan, R. (2022). Analyses of the shutdown system and transients scenarios for the dual fluid reactor concept with metallic molten fuel. *International Journal of Energy Research*, 46.

[Hejzlar et al., 2005] Hejzlar, P., Pope, M. J., Williams, W. C., and Driscoll, M. J. (2005). Gas cooled fast reactor for generation iv service. *Progress in Nuclear Energy*, 47(1):271 – 282.

[Heywood, 2006] Heywood, J. (2006). Viscous incompressible fluids: Mathematical theory. In Françoise, J.-P., Naber, G. L., and Tsun, T. S., editors, *Encyclopedia of Mathematical Physics*, pages 369–379. Academic Press, Oxford.

[Ho and Chu, 1977] Ho, C. Y. and Chu, T. (1977). Electrical resistivity and thermal conductivity of nine selected aisi stainless steels. Technical report, Thermophysical and Electronic Properties Information Analysis Center ....

[Huke et al., 2013] Huke, A., Goetz, R., Hussein, A., Czerski, K., and Gottlieb, S. (Patent WO2013041085A2, May. 2013). Dual fluid reactor.

[Huke et al., 2014] Huke, A., Ruprecht, G., Weißbach, D., Gottlieb, S., Hussein, A., and Czerski, K. (2014). The dual fluid reactor -a new concept for a highly effective fast reactor.

[Huke et al., 2015] Huke, A., Ruprecht, G., Weißbach, D., Gottlieb, S., Hussein, A., and Czerski, K. (2015). The dual fluid reactor – a novel concept for a fast nuclear reactor of high efficiency. *Annals of Nuclear Energy*, 80:225–235.

[Kirkpatrick et al., 1983] Kirkpatrick, S., Gelatt, C. D., and Vecchi, M. P. (1983). Optimization by simulated annealing. *Science*, 220(4598):671–680.

[Laarhoven and Aarts, 1987] Laarhoven, P. J. M. V. and Aarts, E. H. L. (1987). Simulated annealing: Theory and applications. *Springer*, page 7–15.

[Lee and Kim, 2017] Lee, G. H. and Kim, H. R. (2017). Design analysis of dc electromagnetic pump for liquid sodium–co2 reaction experimental characterization. *Annals of Nuclear Energy*, 109:490 – 497.

[Lienhard and Lienhard, 2020] Lienhard, IV, J. H. and Lienhard, V, J. H. (2020). *A Heat Transfer Textbook*. Phlogiston Press, Cambridge, MA, 5th edition. Version 5.10.

[Liu et al., 2022] Liu, S., Zhang, T., and Wang, X. (2022). Steady-state analyses of an smdfr with coupled serpent-openfoam calculation. *Nuclear Engineering and Design*, 396:111892.

[Miao et al., 2023] Miao, Y., Mo, K., Fei, T., and Cao, Y. (2023). Multiphysics simulations of self-regulating performance of an optimized molten metal fuel microreactor design. *Nuclear Engineering and Design*, 406:112244.

[Nowak et al., 2022] Nowak, M., Spirzewski, M., and Czerski, K. (2022). Optimization of the dc magnetohydrodynamic pump for the dual fluid reactor. *Annals of Nuclear Energy*, 174:109142.

[Okamoto, 2012] Okamoto, H. (2012). Cr-u (chromium-uranium). *Journal of Phase Equilibria and Diffusion*, 33(6):495–495.

[Pioro, 2016] Pioro, I. (2016). 2 - introduction: Generation iv international forum. In Pioro, I. L., editor, *Handbook of Generation IV Nuclear Reactors*, Woodhead Publishing Series in Energy, pages 37–54. Woodhead Publishing.

[Polidori, 2010] Polidori, M. (2010). Implementation of thermo-physical properties and thermal-hydraulic characteristics of lead-bismuth eutectic and lead on cathare code.

[Polidori et al., 2012] Polidori, M., Meloni, P., Lombardo, C., Bandini, G., Geffraye, G., and Kadri, D. (2012). Cathare thermal-hydraulic system code for hlm preliminary validation in natural convection tests. *International Congress on Advances in Nuclear Power Plants 2012, ICAPP 2012*, 3:2015–2023.

[Polidori and Kadri, 2012] Polidori, M., M. P. L. C. B. G. G. G. and Kadri, D. (2012). Cathare thermal-hydraulic system code for hlm preliminary validation in natural convection tests.

[Polzin, 2007] Polzin, K. (2007). Liquid metal pump technologies for nuclear surface power. *Marshall Space Flight Center*.

[Provow and Fisher, 1964] Provow, D. and Fisher, R. (1964). The electrical resistivity of solid and molten uranium-chromium eutectic. *Journal of the Less Common Metals*, 6(4):313 – 321.

[Rapp, 2017] Rapp, B. E. (2017). Chapter 9 - fluids. In Rapp, B. E., editor, *Microfluidics: Modelling, Mechanics and Mathematics*, Micro and Nano Technologies, pages 243–263. Elsevier, Oxford.

[Serp et al., 2014] Serp, J., Allibert, M., Ondřej Beneš, Delpech, S., Feynberg, O., Ghetta, V., Heuer, D., Holcomb, D., Ignatiev, V., Kloosterman, J. L., Luzzi, L., Merle-Lucotte, E., Uhlíř, J., Yoshioka, R., and Zhimin, D. (2014). The molten salt reactor (msr) in generation iv: Overview and perspectives. *Progress in Nuclear Energy*, 77:308 – 319.

[Shashi Menon, 2015] Shashi Menon, E. (2015). Chapter five - fluid flow in pipes. In Shashi Menon, E., editor, *Transmission Pipeline Calculations and Simulations Manual*, pages 149–234. Gulf Professional Publishing, Boston.

[Shaver and Wittenbrock, 1967] Shaver, R. E. and Wittenbrock, N. G. (1967). Review of reactor safety analyses of fast and liquid metal cooled reactors.

[Sierchuła et al., 2022] Sierchuła, J., Da˛browski, M. P., and Czerski, K. (2022). Negative temperature coefficients of reactivity for metallic fuel dual fluid reactor. *Progress in Nuclear Energy*, 146:104126.

[Sierchuła et al., 2019] Sierchuła, J., Weissbach, D., Huke, A., Ruprecht, G., Czerski, K., and Da˛browski, M. P. (2019). Determination of the liquid eutectic metal fuel dual fluid reactor (dfrm) design – steady state calculations. *International Journal of Energy Research*, 43(8):3692–3701.

[Singh, 2021] Singh, O. P. (2021). Chapter 12 - nuclear reactors of the future. In Mohanakrishnan, P., Singh, O. P., and Umasankari, K., editors, *Physics of Nuclear Reactors*, pages 695–746. Academic Press.

[Smith et al., 2008] Smith, C. F., Halsey, W. G., Brown, N. W., Sienicki, J. J., Moisseytsev, A., and Wade, D. C. (2008). Sstar: The us lead-cooled fast reactor (lfr). *Journal of Nuclear Materials*, 376(3):255 – 259. Heavy Liquid Metal Cooled Reactors and Related Technologies.

[Thomas, 1999] Thomas, P. (1999). 21 - nuclear reactors. In Thomas, P., editor, *Simulation of Industrial Processes for Control Engineers*, pages 268–281. Butterworth-Heinemann, Oxford.

[Todreas and Kazimi, 2021] Todreas, N. and Kazimi, M. (2021). *Nuclear Systems Volume I: Thermal Hydraulic Fundamentals, Third Edition*. Number t. 1 in Nuclear Systems. CRC Press.

[van Rooijen, 2009] van Rooijen, W. F. G. (2009). Gas-cooled fast reactor: A historical overview and future outlook. *Science and Technology of Nuclear Installations*, 2009:965757.

[Voorde and Division, 1983] Voorde, M. H. V. A. N. D. E. and Division, M. (1983). HIGH-TEMPERATURE MATERIALS. *Commission of the European Communities*, XI.

[Wang et al., 2021a] Wang, J., Apresa, J. A., Weathered, M., Perez, A., and Corradini, M. (2021a). Transient safety evaluation of the heat pipe microreactor – potential energy source for hydrogen production. *International Journal of Hydrogen Energy*, 46(78):38887–38902.

[Wang et al., 2021b] Wang, M., He, X., Macian-Juan, R., and Wang, X. (2021b). One-dimensional transient analysis of the dual-fluid reactor system. *Annals of Nuclear Energy*, 162:108481.

[Wang et al., 2019] Wang, X., Liu, C., and Macian-Juan, R. (2019). Preliminary hydraulic analysis of the distribution zone in the dual fluid reactor concept. *Progress in Nuclear Energy*, 110:364–373.

[Wang and Macian-Juan, 2018] Wang, X. and Macian-Juan, R. (2018). Steady-state reactor physics of the dual fluid reactor concept. *International Journal of Energy Research*, 42(14):4313–4334.

[Watt, 1959] Watt, D. A. (1959). The design of electromagnetic pumps for liquid metals. *Proceedings of the IEE - Part A: Power Engineering*, 106(26):94–103.

[Weissbach et al., 2021] Weissbach, D., Sierchuła, J., Dąbrowski, M. P., Czerski, K., and Ruprecht, G. (2021). Dual fluid reactor as a long-term burner of actinides in spent nuclear fuel. *International Journal of Energy Research*, 45(8):11589–11597.

List of Figures

List of Tables